

Fitting spectral energy distributions of FMOS-COSMOS emission-line galaxies at $z \sim 1.6$: Star formation rates, dust attenuation, and [OIII] $\lambda 5007$ emission-line luminosities

J. A. Villa-Vélez^{1,*}, V. Buat^{1,2}, P. Theulé¹, M. Boquien³, and D. Burgarella¹

¹ Aix Marseille Univ, CNRS, CNES, LAM, Marseille, France

² Institute Universitaire de France (IUF)

³ Centro de Astronomía (CITEVA), Universidad de Antofagasta, Avenida Angamos 601, Antofagasta, Chile

Received March 25, 2021; accepted August 9, 2021

ABSTRACT

We perform a spectral energy distribution fitting analysis on a COSMOS photometric sample covering the ultra-violet up to the far-infrared wavelengths and including emission lines from the Fiber Multi-Object Spectrograph (FMOS) survey. The sample consists of 182 objects with $H\alpha$ and [OIII] $\lambda 5007$ emission line measurements lying in a redshift range of $1.40 < z < 1.68$. We obtain robust estimates of the stellar mass and star-formation rate spanning over a range of $10^{9.5} - 10^{11.5} M_{\odot}$ and $10^1 - 10^3 M_{\odot} \text{ yr}^{-1}$ from the Bayesian analysis performed with CIGALE and using continuum photometry and $H\alpha$ fluxes. Combining photometry and spectroscopy gives secure estimations of the amount of dust attenuation for both continuum and line emissions. We obtain a median attenuation of $A_{H\alpha} = 1.16 \pm 0.19$ mag and $A_{[\text{OIII}] \lambda 5007} = 1.41 \pm 0.22$ mag. $H\alpha$ and [OIII] $\lambda 5007$ attenuations are found to increase with stellar mass, confirming previous findings with $H\alpha$. A difference of 57% in the attenuation experienced by emission lines and continuum is found to be in agreement with the emission lines being more attenuated than the continuum emission. Implementation of new CLOUDY HII-region models in CIGALE enables good fits of the $H\alpha$, $H\beta$, [OIII] $\lambda 5007$ emission lines with discrepancies smaller than 0.2 dex in the predicted fluxes. Fitting the [NII] $\lambda 6584$ line is found challenging due to well-known discrepancies in the locus of galaxies in the [NII]-BPT diagram at intermediate and high redshifts. We find a positive correlation between SFR and $L_{[\text{OIII}] \lambda 5007}$ after correcting for dust attenuation and we derive the linear relation $\log_{10}(\text{SFR}/M_{\odot} \text{ yr}^{-1}) = \log_{10}(L_{[\text{OIII}] \lambda 5007}/\text{ergs s}^{-1}) - (41.20 \pm 0.02)$. Leaving the slope as a free parameter leads to $\log_{10}(\text{SFR}/M_{\odot} \text{ yr}^{-1}) = (0.83 \pm 0.06) \log_{10}(L_{[\text{OIII}] \lambda 5007}/\text{ergs s}^{-1}) - (34.01 \pm 2.63)$. The spread in the relation is driven by differences in the gas-phase metallicity and ionization parameter accounting for a 0.24 dex and 1.1 dex of the dispersion, respectively. We report an average value of $\log U \approx -2.85$ for this sample of galaxies. Including HII-region models to fit simultaneously photometric data and emission line fluxes is paramount to analyses of upcoming data sets from large spectroscopic surveys of the future, such as MOONS and PFS.

Key words. catalogs – galaxies: high-redshift – galaxies: ISM – infrared: galaxies – ISM: dust – extinction

1. Introduction

The spectral energy distribution (SED) of a galaxy from the ultra-violet (UV) to the far-infrared (far-IR) reflects its stellar populations and the interplay of their emitted light with gas and dust in the interstellar medium (ISM). The UV to near-infrared (NIR) emission is the result of stellar populations created over a galaxy's lifetime. Dust absorption of the stellar light leaves its imprint on the gas and the stellar continuum and also via the re-emission of the heated dust in the mid and far-IR. The ionized gas component produced by the high-energy flux of massive stars is studied through the nebular emission of the galaxy, providing access to the very recent star formation of massive stars and physical conditions inside HII-regions.

As a consequence, SEDs over a large range of wavelengths and combining photometric data and emission lines give us access to crucial quantities, such as the current star formation rate (SFR), stellar mass, star formation history (SFH) over different timescales, dust attenuation, dust content, or stellar and gas metallicities. However, the coupling of stars, gas, and dust in a galaxy makes difficult the extraction of the information for each

component. The comparison of models predicting the full SED to observed fluxes from the continuum and line emission has been proven to be very powerful to infer these physical parameters in star-forming galaxy populations (Fossati et al. 2018; Buat et al. 2018; Corre et al. 2018; Yuan et al. 2019). For such comparisons, different categories of models are used. The SFH is either modeled with simple analytical functions or non-parametric forms, or it comes from numerical simulations (semi-analytical or hydrodynamical). The interplay between dust and stars is described either using a radiation transfer modeling with more or less complex configurations or with simpler, phenomenological laws that can sometimes be combined with an energy budget (Silva et al. 1998; Popescu et al. 2000; da Cunha et al. 2008; Boquien et al. 2019). The nebular component is added either using physical modeling with codes such as CLOUDY or MAPPINGS (Ferland et al. 2017; Allen et al. 2008), as in Code Investigating GALaxy Emission (CIGALE¹) (Boquien et al. 2019), Bayesian Analysis of GALaxy sEds (BEAGLE) (Chevallard & Charlot 2016), *ProSpect* package (Robotham et al. 2020), Python code for Stellar Population Inference from Spectra and SEDs (Prospector) (Leja et al. 2017; Johnson et al. 2021), Bayesian

* E-mail: jorge.villa@lam.fr

¹ <https://cigale.lam.fr/>

Analysis of Galaxies for Physical Inference and Parameter Estimation (Bagpipes) (Carnall et al. 2018), *MCESED* (Bowman et al. 2020), or with empirical relations relating different emissions as in PHotometric Analysis for Redshift Estimations (lePHARE) (Arnouts et al. 1999; Ilbert et al. 2006). Some SED fitting codes are capable of combining continuum and emission line fluxes when the analysis of data obtained with new facilities will require the handling of very large data sets and the modeling of very different galaxy populations (Ellis et al. 2017; Thorne et al. 2021).

The IR emission is crucial with regard to putting constraints on stellar obscuration (Buat et al. 2018) and to estimate physical quantities as the SFR of galaxies from the energy budget (Smith et al. 2012; Małek et al. 2018; Nersesian et al. 2019; Dobbels et al. 2020). We note that the modeling of the infrared (IR) dust emission is not included in all the SED fitting codes; CIGALE includes three different sets of models from Draine & Li (2007), with updates of Draine et al. (2014), Casey (2012), and Dale et al. (2014), while Prospector, Bagpipes, ProSpect and BEAGLE only include one of the aforementioned sets. Moreover, active galactic nuclei (AGN) templates from Fritz et al. (2006), Casey (2012), and Dale et al. (2014) are also available in CIGALE and ProSpect where the former also includes Andrews et al. (2018) templates. Nevertheless, emission line models are still not available for use with the AGN templates. Large spectro-photometric surveys on 8-meter telescopes will provide thousands to millions of spectra in the deepest photometric fields, such as with the Multi-Object Optical and Near-infrared Spectrograph (MOONS) for the Very Large Telescope (VLT) and the Subaru Prime Focus Spectrograph (PFS), and larger facilities (e.g., Extremely Large Telescope) such as the Multi-Object Spectrograph for Astrophysics, Intergalactic-medium studies, and Cosmology (MOSAIC). The James Webb Space Telescope (JWST) will push the observations of both rest-frame UV-optical continuum and emission lines to very high redshift in particular the $H\alpha$ and [OIII] λ 5007 emission lines for which different physical conditions and configurations will need to be taken into account in their modeling (Schaerer & de Barros 2009; Wright et al. 2015; Wells et al. 2015; Álvarez-Márquez et al. 2019; Chevallard et al. 2019). While treating both photometric and emission line information simultaneously, it is important to account for the potential contribution of emission lines in photometric bands, which can substantially modify the observed fluxes increasing the uncertainties in the parameter estimations (Schaerer & de Barros 2010; Stark et al. 2013; Tang et al. 2021). The coupling of multi-wavelength data sets in the SED fitting including emission lines and a good treatment of the IR emission remains paramount in the work to characterize, derive, and accurately measure the properties of galaxies.

In this paper, we attempt to simultaneously fit photometric and spectroscopic data with CIGALE in the Cosmic Evolution Survey (COSMOS) field using photometry from Laigle et al. (2016) and emission line fluxes from the Fiber Multi-Object Spectrograph (FMOS-COSMOS) survey (Kashino et al. 2013; Silverman et al. 2015). This work has multiple aims as we want to test the consistency of both types of data (photometric and spectroscopic) to derive SFR, stellar mass, and dust attenuation for both the lines and continuum. The conservation of the energy budget by CIGALE allows us to get robust estimates of the amount of dust attenuation. In order to get both $H\alpha$ and [OIII] λ 5007 fluxes with good quality, the redshift range is reduced to $1.40 < z < 1.68$. We fit the photometry and $H\alpha$ flux emission to constrain the attenuation and correct emission line luminosities for dust effects. We focus our study on understand-

ing the SFR-[OIII] λ 5007 relation, and the influence of metallicity and ionization field. In the FMOS-COSMOS catalog, we have access to other emission lines as $H\beta$ and [NII] λ 6584, which are used to emphasize the difficulties in HII-region modeling and coupling these models with SED fitting methods.

The data selection is presented in Sect. 2. The wavelength coverage of the photometric data goes from the UV to the far-IR including emission lines fluxes from the FMOS-COSMOS survey. We fit the $H\alpha$ emission line flux and photometric data to measure SFR and stellar mass and put our sample in a SFR- M_{star} diagram, the SED fitting analysis, and its results are presented in Sect. 3. Dust attenuation for both stellar continuum and emission lines are discussed in Sect. 4 and we study the SFR-[OIII] λ 5007 relation in Sect. 5. In Sect. 6, we add other lines to the fitting analysis and discuss the ability of extended CLOUDY models to fit the full set of data. Finally, in Sect. 7, we summarize the main parts of this work and conclusions. This work assumes a flat seven-year Wilkinson Microwave Anisotropy Probe (WMAP7) cosmology (Komatsu et al. 2011) with $h = 0.704$, $\Omega_{\Lambda} = 0.727$, and $\Omega_{\text{M}} = 0.273$, AB magnitudes, and a Chabrier (2003) initial mass function (IMF).

2. Data selection

2.1. UV-to-NIR Photometry

The COSMOS field covers 2 deg^2 and is centered at $\alpha(\text{J2000}) = 10^{\text{h}}0^{\text{m}}27.9^{\text{s}}$ and $\delta(\text{J2000}) = 0^{\text{h}}8^{\text{m}}50.3^{\text{s}}$ (Scoville et al. 2007). We adopt the multi-wavelength catalog of Laigle et al. (2016), COSMOS2015, containing photometry from Galaxy Evolution Explorer near ultra-violet (GALEX NUV) as well as U, B, V, r, i, z, y, J, H, and K_s , and the *Spitzer* Infrared Array Camera (IRAC) 3.6, 4.5, 5.8, and $8.0 \mu\text{m}$ photometry from Canada France Hawaii Telescope (CFHT) MegaCam and Wide-field InfraRed Camera (WIRCam), SUBARU Prime Focus Camera (Suprime-Cam) and Hyper Suprime-Cam (HSC), and United Kingdom Infra-Red Telescope (UKIRT) Wide Field Infrared Camera (WFC), and *Spitzer*, respectively. The NUV fluxes overlapping the Lyman break are discarded. This corresponds to sources with $z > 1.5$ at the GALEX NUV filter's effective wavelength of $\lambda_{\text{eff}} = 2304.74 \text{ \AA}$.

2.2. *Spitzer* MIPS and *Herschel* PACS and SPIRE data

For the IR range, we accessed data from the *Herschel* Extragalactic Legacy Project (HELP²). We used the *Spitzer* Multi-Band Imaging Photometer (MIPS) $24 \mu\text{m}$, *Herschel* Photodetector Array Camera and Spectrometer (PACS) 100 and $160 \mu\text{m}$, and *Herschel* Spectral and Photometric Imaging REceiver (SPIRE) 250, 350, $500 \mu\text{m}$ data products.

Spitzer MIPS and *Herschel* PACS and SPIRE fluxes are the result of the HELP XID+ extraction based on the position of priors; XID+ uses a Bayesian probabilistic framework that includes priors to measure fluxes and their uncertainties (Hurley et al. 2017).

Both *Spitzer* MIPS $24 \mu\text{m}$ and *Herschel* PACS 100, and $160 \mu\text{m}$ were obtained using *Spitzer* IRAC sources from the *Spitzer* Large Area Survey with the Hyper-Suprime-Cam (SPLASH; Capak et al. 2012) as positional priors. In the case of *Herschel* SPIRE 250, 350, $500 \mu\text{m}$, XID+ was run using $24 \mu\text{m}$ priors from Le Floc'h et al. (2009) catalog with the addition of the Submillimetre Common-User

² <https://herschellegacyproject.wordpress.com/>

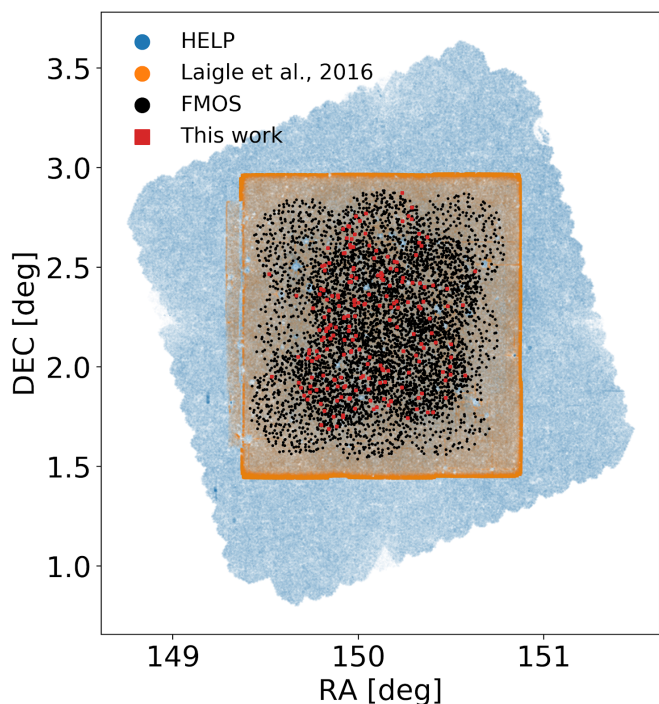


Fig. 1. Spectro-photometric sample. In blue, we show the position for objects in the HELP-project catalog. In orange, the main bulk of photometry from the COSMOS2015 catalog (Laigle et al. 2016). In black, the FMOS-COSMOS emission line targets. In red, the final selection for this work.

Bolometer Array 2 (SCUBA-2) radio and Atacama Large Millimeter/submillimeter Array (ALMA) data. The products corresponds to *Spitzer* MIPS ‘dmu26_XID+MIPS_COSMOS’, *Herschel* PACS ‘dmu26_XID+PACS_COSMOS’, and *Herschel* SPIRE ‘dmu26_XID+SPIRE_COSMOS’ available in the merged version ‘dmu32_COSMOS’ at the HELP-repository³. Further information can be found in the Github repository of the project⁴.

2.3. FMOS-COSMOS emission lines

The Fiber Multi-Object Spectrograph (FMOS) is an instrument located at the Subaru telescope at the Mauna Kea Observatory in Hawaii. The instrument is a fiber-fed system that allows for wide-field spectroscopy and enabling NIR spectroscopy. We used data from the FMOS-COSMOS survey as described in Kashino et al. (2013) and Silverman et al. (2015) for the emission line fluxes. These observations were performed using FMOS in high-resolution (HR) mode. It contains $H\alpha$, $H\beta$, [NII] λ 6584, [OIII] λ 5007, [SII] λ 6717, and [SII] λ 6731⁵ emission line fluxes. We selected objects with at least $H\alpha$ and [OIII] λ 5007 flux measurements, limiting the redshift range to $1.38 < z < 2.6$ in which both lines are observable by FMOS. Aperture corrections were applied following the prescriptions of Kashino et al. (2019). To guarantee a good level of quality for the $H\alpha$, [NII] λ 6584, $H\beta$, and [OIII] λ 5007 spectral lines, we selected catalog sources with spectral fits obtained using a single Gaussian

model (Silverman et al. 2015). We only considered emission lines detected with a signal-to-noise ratio (S/N) larger than 3. The measurement error in the emission line corresponds to the formal error provided by the line fitting process. The aperture correction value provided for each object is the best value derived from three different methods (see Kashino et al. 2019) and is used to correct in-fiber measurements. We keep only objects for which the flux loss is lower than 70%. To calculate the full uncertainty (fitting process and aperture correction) the formal errors on the observed emission line must be added up in quadrature, with a suggested factor of 1.5 from Kashino et al. (2019), to account for the uncertainty introduced by the aperture correction.

2.4. Final sample selection

We started with a sample of 1182108 galaxies from the COSMOS2015 catalog, which was reduced to 199 once it was cross-matched to the available IR data from the HELP-project and the FMOS-COSMOS catalog. The different data sets used in this work are represented in Fig. 1. In Fig. 2, the normalized transmission curves of each photometric filter used to estimate the modeled flux densities are presented (see Sect. 2.1 and Sect. 2.3).

A total of 182 objects were selected on the basis of their flux measurements for both $H\alpha$ and [OIII] λ 5007 with $S/N > 3$. In Fig. 3, the final sample redshift distribution covering $1.4 < z < 1.68$ is presented. This selection is shown in Fig. 1 as red dots over imposed on the FMOS-COSMOS sample (black dots), the COSMOS2015 catalog from Laigle et al. (2016), and the HELP-project data. The number of objects per band is shown in Table 1. S/N drops for *Herschel* PACS and *Herschel* SPIRE bands, leading to 43 and 15 objects with $S/N > 3$ at $100 \mu\text{m}$, and $160 \mu\text{m}$, and 50, 35, and 0 objects for the *Herschel* SPIRE bands 250, 350, and $500 \mu\text{m}$, respectively. Our entire sample has a $S/N > 3$ in the *Spitzer* MIPS $24 \mu\text{m}$, *Spitzer* IRAC1 $3.6 \mu\text{m}$, and *Spitzer* IRAC2 $4.5 \mu\text{m}$ bands, but drops for *Spitzer* IRAC3 $5.8 \mu\text{m}$ and *Spitzer* IRAC4 $8.0 \mu\text{m}$ with 95 and 44 objects, respectively. Individual poorly measured photometric data does not affect the SED fitting result because the weight of these bands in the overall fit is small due to their large measurement error.

Most of the sample includes UV-to-MIR photometry and $H\beta$, [NII] λ 6584, [SII] λ 6717, and [SII] λ 6731 emission line fluxes. The quality of the measure of the flux is assessed by the S/N . Of the 139 objects that have data for the $H\beta$ and [NII] λ 6584 emission lines, 114 and 112 sources have a $S/N > 3$, respectively. [SII] λ 6717 and [SII] λ 6731 emission line measurements are of very poor quality, leading only to 22 and 15 objects with a $S/N > 3$. The quality of the $H\beta$ measurements in terms of the Balmer Decrement (BD) will be addressed in Sect. 4. In Sect. 6, we present a more detailed study of the emission lines.

We need to avoid any possible contamination due to an AGN contribution. Kashino et al. (2017) flagged AGN in the FMOS-COSMOS sample as point sources with an associated X-ray emission provided by the *Chandra*-COSMOS Legacy survey catalog (Elvis et al. 2009; Civano et al. 2016) with $L_{X\text{-ray}} \geq 10^{42} \text{erg s}^{-1}$ at $0.5 - 0.7 \text{keV}$. Any source flagged as being associated with X-ray emission was discarded from our main sample. Obscured AGN contamination is still possible even if X-ray detected sources are excluded. Kashino et al. (2017) identified 39 objects consistent with obscured (type-II) AGN based on narrow line ratios, with only four of those objects having an X-ray counterpart. Nevertheless, we did not exclude these objects from our analysis because our results are robust enough even if these ob-

³ http://hedam.lam.fr/HELP/dataproducts/dmu32/dmu32_COSMOS/

⁴ https://github.com/H-E-L-P/dmu_products.

⁵ The [SII] λ 6717 and [SII] λ 6731 data are a private communication of the authors (Kashino & Silverman)

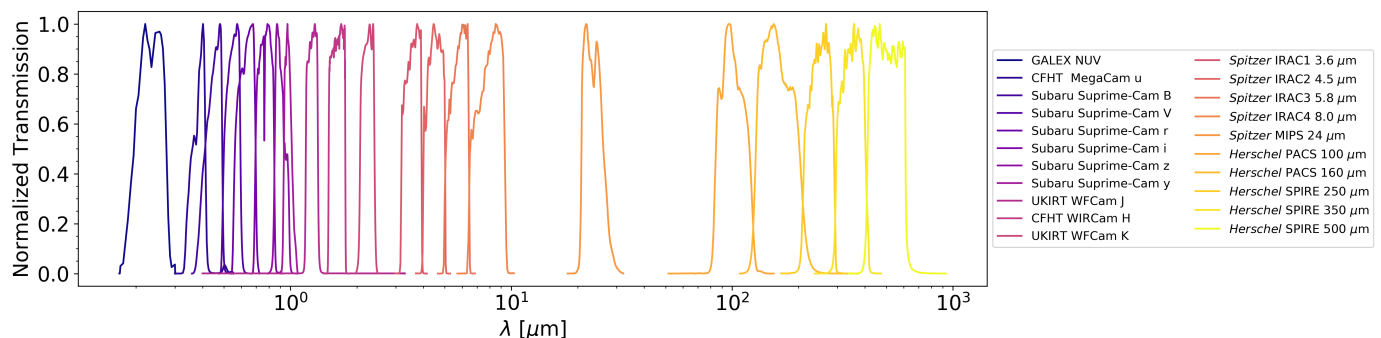


Fig. 2. Normalized transmission curves of photometric filters used in CIGALE to estimate the modeled flux densities in each band for the FMOS-COSMOS sample. The list of the filters is shown on the right side.

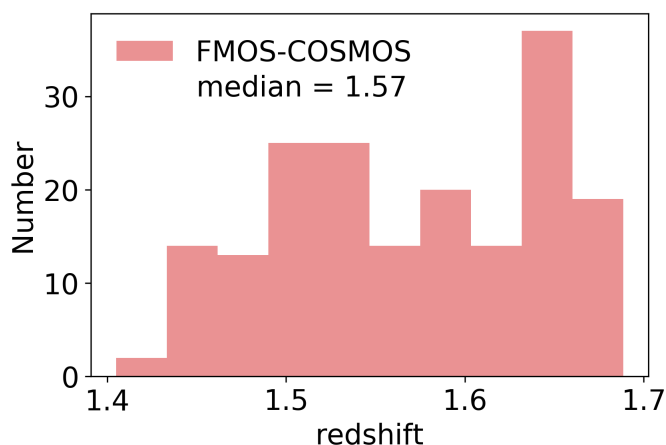


Fig. 3. Redshift distribution of the 182 FMOS-COSMOS selected sources. The sample has a median of 1.57 for the redshift.

jects are included probably because they are not extreme cases. We used the color criteria of Donley et al. (2012) to separate AGN from star-forming galaxies and verify that none of our objects lie inside the AGN region.

3. SED fitting with CIGALE

In this section, we present the SED fitting process carried out with the code CIGALE (Boquien et al. 2019). Here, we describe the modules that we use and their direct impact on the analysis of our data set. The structure of the code is addressed by different authors in the literature (e.g., Ciesla et al. 2017; Małek et al. 2018; Buat et al. 2018; Boquien et al. 2019). CIGALE is based on the energy balance principle in which dust partially absorbs emission of all origins in the UV-optical wavelength range and re-emits this energy in the IR. The code creates millions of models to be compared with the observations and estimates physical parameters of galaxies (such as SFR, stellar mass, dust luminosity, dust attenuation, AGN fraction) while applying a Bayesian statistical analysis approach.

Different modules were chosen from the CIGALE library to model the star-formation history (SFH), the nebular emission, the dust attenuation, and re-emission. The parameters and their uncertainties are computed using the goodness of fit for all the models as a likelihood-weighted mean and likelihood-weighted standard deviation, respectively. A global indicator of the quality of the fits is given by the reduced χ^2 (χ_r^2). In general, the χ_r^2 must account for the degrees of freedom, however, the non-linearity

Table 1. Final sample. Number of objects per band and $S/N > 3$. Emission lines marked with a star are the result of private communication with the authors (Kashino & Silverman).

Bands	Data	$> 3\sigma$
GALEX NUV	51	13
CFHT MegaCam u	182	181
Subaru Suprime-Cam B	183	183
Subaru Suprime-Cam V	183	183
Subaru Suprime-Cam r	183	183
Subaru Suprime-Cam i	183	183
Subaru Suprime-Cam z	183	183
Subaru Suprime-Cam y	183	182
UKIRT WFCam J	182	182
CFHT WIRCam H	182	182
UKIRT WFCam K	182	182
<i>Spitzer</i> IRAC1 3.6 μm	183	183
<i>Spitzer</i> IRAC2 4.5 μm	183	183
<i>Spitzer</i> IRAC3 5.8 μm	173	95
<i>Spitzer</i> IRAC4 8.0 μm	128	44
<i>Spitzer</i> MIPS 24 μm	183	183
<i>Herschel</i> PACS 100 μm	183	43
<i>Herschel</i> PACS 160 μm	183	15
<i>Herschel</i> SPIRE 250 μm	81	50
<i>Herschel</i> SPIRE 350 μm	81	35
<i>Herschel</i> SPIRE 500 μm	81	0

Emission line	Data	$> 3\sigma$
FMOS H α	183	182
FMOS H β	139	114
FMOS [NII] λ 6584	139	112
FMOS [OIII] λ 5007	183	182
FMOS [SII] λ 6717*	40	22
FMOS [SII] λ 6731*	35	15

of the equations (Chevallard & Charlot 2016) linking the parameters and their non-trivial dependence on each other makes it difficult to include them. Therefore, the χ_r^2 corresponds to the χ^2 divided by the total number of input fluxes.

The combination of H α fluxes with UV-to-IR data with the preservation of the energy budget allows us to get reliable estimates of dust attenuation (see Sect. 3.3) without resorting to other methods such as the Balmer Decrement (BD). It also allows for secure estimations of the SFR to be obtained. Although we have H β , [NII] λ 6584, [OIII] λ 5007, [SII] λ 6717, and [SII] λ 6731 information, we did not fit these lines due to current discrepancies concerning the HII-region models (see Sect. 6) and

to the poor quality of the data, as presented in Sect. 2.4 and Table 1. In particular, the H β fluxes were discarded either because of their low S/N or a H α /H β ratio below the canonical value of 2.86 (see Sect. 4). [NII] λ 6584, [SII] λ 6717, and [SII] λ 6731 only satisfy the S/N criterion for 112, and 22, and 15 objects, respectively. The relevant CIGALE modules selected for this work are introduced in the next sections.

3.1. Star-formation history

We used a delayed SFH with the functional form presented in Eq. 1. This form depends on the time of the star-formation onset, t_0 , and the e-folding time of the stellar population, τ_{main} . A recent burst of constant star formation that has been going for at most 70 Myr is superimposed to the delayed SFH. This form allows us to have a variation of the SFH where the SFR increases from the onset of star-formation until its peak at τ_{main} . After that point, the SFR starts declining:

$$\text{SFR}_{\text{main}}(t) \propto \frac{t}{\tau_{\text{main}}^2} \times \exp(-t/\tau_{\text{main}}) \text{ for } 0 \leq t \leq t_0. \quad (1)$$

The delayed component allows us to add a burst that we define with constant amplitude over the last years (Corre et al. 2018; Carnall et al. 2019; Leja et al. 2019; Chevallard et al. 2019; Buat et al. 2019). The amplitude of the burst is fixed by f_{burst} , defined as a mass ratio between the stars formed during the burst and the total mass of stars. As we select objects with emission lines, we expect the amplitude of the burst to have a direct impact on the derivation of SFR for at least some objects in our sample. The SFR is averaged over 10 Myr compatible to the timescale traced by H α . The input parameters are described in Table 2, where the e-folding time and the age of the main stellar population are left as free parameters as well as the age and the mass fraction of the burst. We used a Chabrier (2003) IMF at solar metallicity 0.02 for the stellar population. Effects on the variation of the estimated parameters due to a fixed stellar metallicity are discussed in Sect. 3.4.

3.2. Nebular emission lines

CIGALE models the galaxy's emission of the ionized gas by stellar generations as an effective HII-region, encompassing the ensemble of HII-regions and the diffuse ionized gas. The nebular emission lines are pre-computed in the nebular module of CIGALE and re-scaled with the number of Lyman continuum photons from the stellar emission of the model galaxy.

The radiation field intensity is given by the dimensionless ionization parameter $\log U \equiv \log(n_\gamma/n_H)$, where n_γ is the number density of photons capable of ionizing hydrogen and n_H the number density of hydrogen. The photo-ionizing field is generated with the single stellar population (SSP) model library of Bruzual & Charlot (2003), using a constant SFH over 10Myr. In Sect. 6, we detail the major changes made in modeling nebular emission as compared to the previous version described in Boquien et al. (2019). The updated version of the HII-region models is used alongside this work to fit photometry and emission line fluxes. Our main purpose is to measure dust attenuation and SFR and to compare the latter to [OIII] λ 5007 luminosities. The new photoionization models allow us to interpret the locus of our galaxies in the excitation diagrams in an attempt to understand the underlying physics of the ISM.

3.3. Dust attenuation recipe and dust emission

We adopted the recipe proposed by Charlot & Fall (2000) (CIGALE module called `dustatt_modified_CF00`; hereafter CF00), where two stellar populations are considered: young stars (age < 10⁷ years) that are still located in a birth cloud (BC), while older stars (age > 10⁷ years) have already moved into the interstellar medium (ISM). Both populations experience a different dust attenuation: the emission of young stars goes through the BC and the ISM while the emission of older stars is only attenuated by dust located in the ISM. The dust attenuation in the ISM and the BC are both modeled as power laws normalized to the amount of attenuation in the V-band ($\lambda_V = 0.55\mu\text{m}$):

$$A_\lambda^{\text{BC}} = A_V^{\text{BC}} (\lambda/\lambda_V)^{n^{\text{BC}}}, \quad (2)$$

$$A_\lambda^{\text{ISM}} = A_V^{\text{ISM}} (\lambda/\lambda_V)^{n^{\text{ISM}}}. \quad (3)$$

The ratio of the attenuation in the V-band experimented by the young and old stars is given by:

$$\mu = A_V^{\text{ISM}} / (A_V^{\text{ISM}} + A_V^{\text{BC}}), \quad (4)$$

where μ is considered as a free parameter in our fitting process (da Cunha et al. 2008; Battisti et al. 2019). Nebular lines coming from the Lyman continuum photons due to very young stars are attenuated as young stars (BC+ISM). The range for each parameter used in the CIGALE's attenuation module is given in Table 2.

The slopes of the two power-laws (i.e., BC and ISM) are fixed to -0.7 following Charlot & Fall (2000). This value reproduces the observed mean relation between the IRX and UV spectral slope of nearby starburst galaxies. Lo Faro et al. (2017), Wild et al. (2007), da Cunha et al. (2008), and Battisti et al. (2019) set $n^{\text{BC}} = -1.3$ to account for effects introduced in the absorption curve due to the optical properties of dust grains as those present in the Milky Way and the Large, and Small Magellanic clouds. However, it has been shown from HII-region studies (see Caplan & Deharveng 1986; Liu et al. 2013) that grayer values closer to the one chosen in this work are more suitable for reproducing the effective attenuation in dusty galaxies. Letting n^{BC} free is not suitable because we use only one emission line and its value would be poorly constrained. In Sect. 4, we explore the effects of changing -0.7 to -1.3 for n^{BC} . The only free parameters in our recipe are μ and A_V^{ISM} . The μ parameter relates the undergone attenuation in the V-band by the ISM (i.e., old stars, continuum) and the BC+ISM (i.e., young stars, emission lines). Leaving μ free to vary allows for some variation on the effective attenuation law (Battisti et al. 2016; Buat et al. 2018; Małek et al. 2018; Chevallard et al. 2019). Moreover, introducing this flexibility in the SED fitting process allows for a better quality fit of the H α emission. Variations of the attenuation law will be explored as further work. The dust emission was fitted with the Draine & Li (2007) models based on a set of parameters to constrain the starlight intensity and link dust to star-formation including updates of Draine et al. (2014). We used these models because we have 24 μm information making them better suited and more flexible for our purpose.

3.4. Spectral energy distribution fitting results

We fit the SEDs of our sample using a set of parameters obtained from previous works and summarized in Table 2. We analyzed

Table 2. CIGALE modules and input parameters used for the SED fitting process as presented in Boquien et al. (2019)

Parameter	Symbol	Range
Delayed Star Formation History and Recent Burst		
e-folding time of main stellar population (Myr)	τ_{main}	1000.0, 3000.0, 4000.0
age of main stellar population (Myr)	age_{main}	2000.0, 2500.0, 3500.0, 4000.0
age of the late burst (Myr)	$\text{age}_{\text{burst}}$	10.0, 40.0, 70.0
mass fraction of the late burst population	f_{burst}	0.0, 0.001, 0.05, 0.1, 0.15
Stellar Populations		
Stellar population synthesis models from Bruzual & Charlot (2003)		
initial mass function	IMF	Chabrier
metallicity	Z_{star}	0.02
Nebular Emission		
ionization parameter	$\log U$	-4.0, -3.5, -3.0, -2.5, -2.0, -1.5, -1.0
gas metallicity	Z_{gas}	0.008, 0.006, 0.01, 0.02, 0.03, 0.04, 0.05
Dust attenuation		
Templates based on values adopted by Charlot & Fall (2000); Buat et al. (2018)		
ISM attenuation in the V-band (mag)	$A_{\text{V}}^{\text{ISM}}$	0.0, 0.3, 0.5, 0.7, 0.9, 1.1, 1.3, 1.5, 1.7, 1.9
$A_{\text{V}}^{\text{ISM}}/(A_{\text{V}}^{\text{ISM}}+A_{\text{V}}^{\text{BC}})$	μ	0.1, 0.3, 0.5, 0.7, 1.0
slope of the attenuation in the ISM	n_{ISM}	-0.7
slope of the attenuation in the BC	n_{BC}	-0.7
Dust Emission		
Templates based on average values following Malek et al. (2018) and references therein		
mass fraction of PAH	q_{PAH}	0.47, 1.12, 1.77, 2.5
minimum radiation field	U_{min}	5.0, 10.0, 25.0
powerlaw slope $dU/dM \propto U^{\alpha}$	α	2.0
fraction illuminated from U_{min} to U_{max}	γ	0.02

the quality of the fits, using the global χ^2 and also comparing the Bayesian estimate of each flux with the observed values. In Fig. 4, the distribution of the obtained χ^2 and χ_r^2 are shown. For each filter, we computed the median value of the difference between the Bayesian estimate from CIGALE and the observed values of fluxes with S/N > 3. Their distribution is presented in Fig. 5. The SED-modeled $H\alpha$ fluxes are presented in Fig. 6 as a function of the observed flux as well as the flux difference ($H\alpha_{\text{CIGALE}} - H\alpha_{\text{FMOS}}$).

From Fig. 5, it is clear that the fluxes are well fitted by CIGALE with a flux difference lower than 0.1 dex and dispersion lower than 0.13 dex except for GALEX NUV for which the dispersion reaches 0.28 dex. *Herschel* PACS 100 μm and 160 μm are underestimated and exhibit a larger dispersion of 0.37 dex and 0.31 dex, respectively. ONLY 43 objects have S/N > 3 in *Herschel* PACS 100 μm . 23 objects have 100 μm fluxes larger than their respective flux at 160 μm . This is an unrealistic configuration at $z \sim 1.5$ with rest-frame fluxes 40 and 60 μm , respectively. The dispersion of the results in *Herschel* PACS bands can be reduced (e.g., red squares in Fig. 5) if we consider the sample of 9 objects with S/N > 3 in both *Herschel* PACS 100 μm and *Herschel* PACS 160 μm . Therefore, the overall bad results at *Herschel* PACS bands can be explained as a combined effect of low S/N and non-realistic configuration at the IR bands. We used a deblended IR catalog in the COSMOS field provided by (Jin et al. 2018) to check if the situation for these bands could be improved. Both data sets (i.e., HELP and Jin et al. 2018) are consistent for our sample with the same trends in terms of the unrealistic configuration of *Herschel* PACS 100 μm and *Herschel* PACS 160 μm . The Jin et al. (2018) data have even lower S/N than our final sample selection (described in Sect. 2.4). Using HELP data for our sample leads to better results for the fits. CIGALE weighs the data as the inverse square of the error, which means that even if flux with a low S/N is badly fitted, its impact on the overall SED fitting output is minimal. We also fit our sources without the *Herschel* PACS and SPIRE bands to check whether SFR, stellar mass, and attenuation estimations are affected when IR data are excluded. The retrieved estimates with and without IR information are consistent with each other within 1σ uncertainty. The impact of *Herschel* SPIRE data on the SFR as compared to the *Herschel* PACS bands is larger (i.e., 0.15 dex). In both cases, the difference in attenuation is larger (3 \times) for [OIII] λ 5007 than

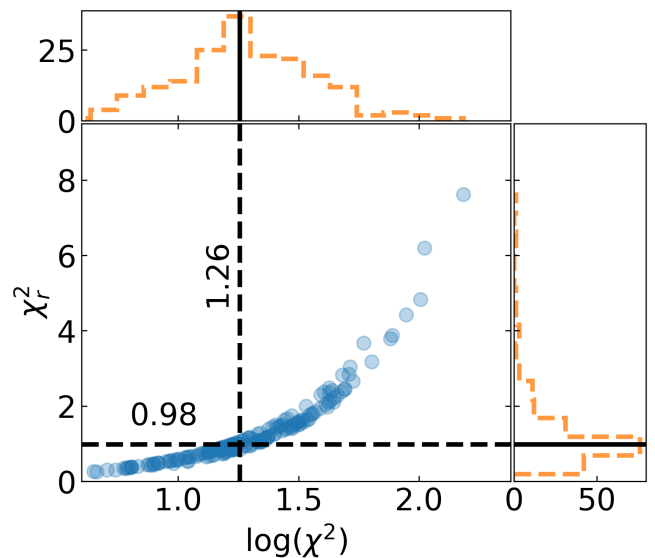


Fig. 4. Reduced χ_r^2 versus the χ^2 . The upper and right panels show the distribution of each parameter while the blue points corresponds to objects in our sample selection. The black lines correspond to the mean value of 0.98 and 1.26 in each case.

for $H\alpha$. We kept the *Herschel* data for the whole sample in the overall fit. In Fig. 6, the Bayesian values of the $H\alpha$ fluxes and the FMOS measurements follow the 1:1 relation, indicating that we are able to fit the line flux very well within a 0.2 dex scatter, as already found by Buat et al. (2018) on a smaller sample in the same field using spectroscopic information from the 3D-HST survey.

Accurate determination of SFRs is crucial as we want to compare them with the [OIII] λ 5007 luminosities. Stellar masses and SFRs retrieved from the SED fitting cover a range of $10^{9.5} - 10^{11.5} M_{\odot}$, and $10^1 - 10^3 M_{\odot} \text{ yr}^{-1}$, respectively. Current high SFRs can be expected for some objects since our sample is selected on the detection of recombination lines. To confirm the need to add a burst the delayed SFH we performed a fit with a burst amplitude set to 0. We compared both fits by calculating the Bayesian Information Criterion (BIC) of each of them as

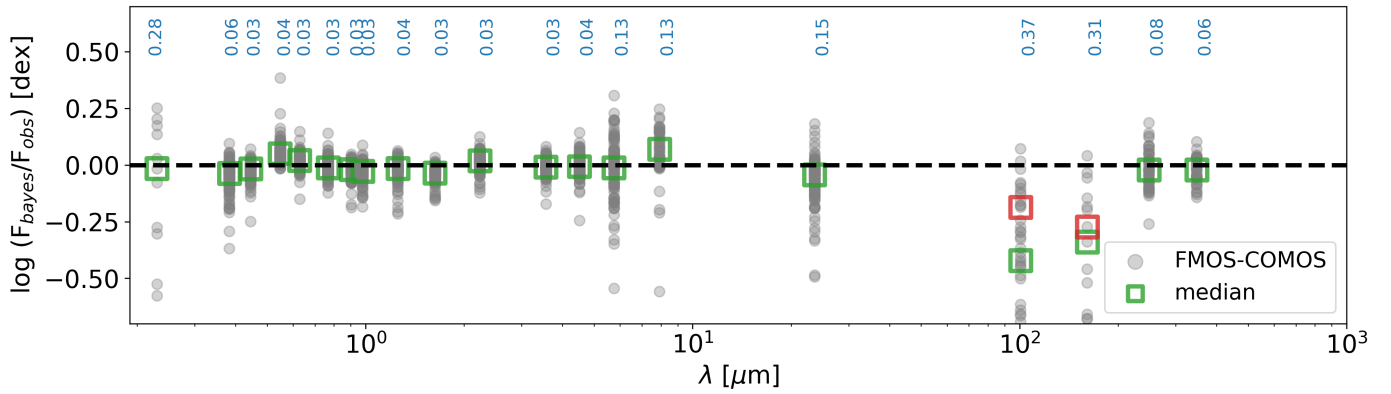


Fig. 5. Median distribution of the SED estimated and observed fluxes. On the x-axis, each wavelength corresponds to the photometric bands used in the SED fitting. The difference between the computed Bayesian flux with CIGALE and the observations is shown in the y-axis. Each object in our sample is drawn as a gray dot with a S/N > 3 in each band. Median values are shown as green squares. The median values for objects with S/N > 3 in both *Herschel* PACS 100 μ m and *Herschel* PACS 160 μ m are presented as red squares. Dispersion on the flux difference at each wavelength is reported on top.

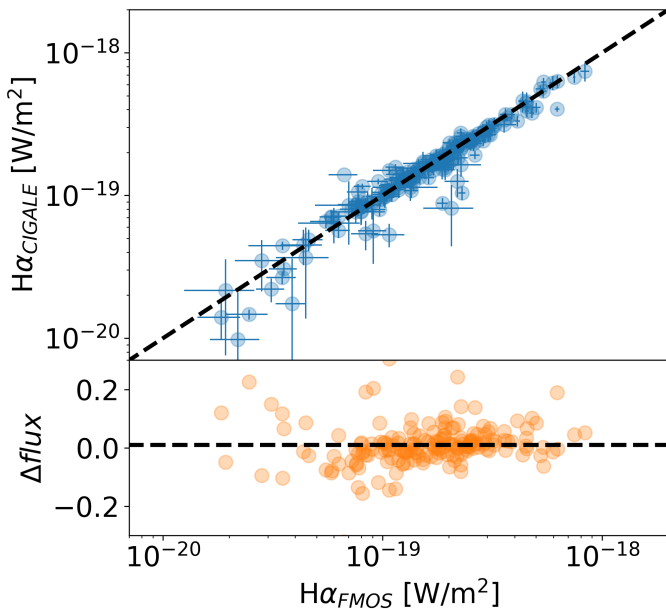


Fig. 6. Fit quality of the $H\alpha$ emission line. The upper panel shows the computed Bayesian flux using CIGALE on the y-axis vs the FMOS measured flux in the x-axis. The 1:1 relation is shown as a dashed line. The relative difference in flux is presented in the lower panel in logarithmic scale. Bayesian and measured errors are shown for CIGALE and FMOS $H\alpha$ fluxes, respectively. The differences between the computed flux with CIGALE and the observed data are not larger than 0.2 dex.

introduced by Schwarz (1978) and defined as:

$$\text{BIC} = -2 \times \ln(\text{likelihood}) + \kappa \times \ln(N),$$

where N stands for the number of observations namely, the number of bands fitted, κ the number of degrees of freedom, and $\chi^2 = -2 \times \ln(\text{likelihood})$ the non-reduced χ^2 obtained from CIGALE (Ciesla et al. 2017; Buat et al. 2018). A significant difference and evidence against a model is characterized by the higher BIC. We computed the difference of BIC values $\Delta(\text{BIC})$. As the number of bands fitted is the same in both cases, any difference arises from the number of degrees of freedom ($\kappa_{\text{fix}} = 14$ and $\kappa_{\text{free}} = 16$) and the χ^2 . $\Delta(\text{BIC}) > 2$ for 90 ($\Delta(\text{BIC}) > 6$ for 69) objects, meaning that for 1/3 to 1/2 of our sample the

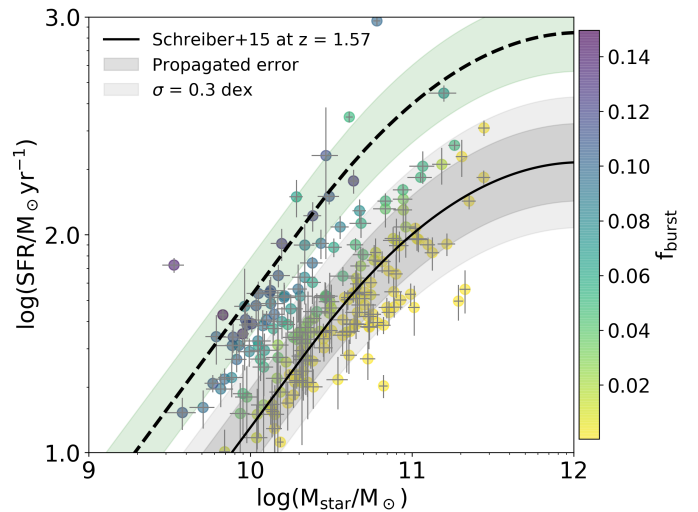


Fig. 7. Star-formation rate versus stellar mass diagram. The dashed line corresponds to the Schreiber et al. (2015) curve evaluated at a median sample redshift of $z = 1.5$. The propagated error dispersion from the fitted errors of the function and a 0.3 dex scatter usually found for the relation in literature are shown as shades. Objects are color-coded by the mass fraction of the late burst population (f_{burst}). Galaxies four times above the main-sequence (black solid line) are consistent with a SED validated starburst population ($f_{\text{burst}} \sim 0.1$) within the 1σ dispersion shown as green shade area. Bayesian error for SFR and stellar mass are reported.

introduction of a burst improves the fit. In Fig. 7, our sample is presented in the SFR-mass diagram color-coded with f_{burst} . The Schreiber et al. (2015) main-sequence relation for a redshift of $z = 1.5$ is drawn with a 0.3 dex dispersion (Karim et al. 2011; Rodighiero et al. 2011). The dispersion computed by error propagation from the originally fitted parameter errors is also shown as a darker shaded contour. The bulk of galaxies is found to lie within the 0.3 dex curves. Galaxies four times above the main-sequence are usually considered starbursting (Sargent et al. 2012). A total of 31 objects in our sample are consistent to be starbursts with $f_{\text{burst}} > 0.06$ within a 1σ dispersion. The median value of f_{burst} for these objects is 0.10 ± 0.03 . We fit the data using a stellar continuum metallicity of 0.008 and confirm that the re-

sults are consistent with the 0.02 case. Variations are within 1σ dispersion for the stellar mass, SFR, and attenuation estimates.

4. Dust attenuation

As noted above, we simultaneously fit the photometric and spectroscopic data (i.e., $H\alpha$ fluxes) using the [Charlot & Fall \(2000\)](#) modified recipe. Emission lines are produced by excited gas inside the BC as a result of the emitted radiation by young stars. Therefore, the lines suffer from attenuation due to the BC and by the ISM surrounding the HII-region.

The combination of the energy budget principle of stellar photons being absorbed and re-emitted by dust in the Mid-and-far-IR with the attenuation recipe allows us to measure the net effect of dust obscuration (i.e., the effective attenuation) in our galaxy sample. CIGALE calculates the resulting attenuation at any wavelength and for any emission line allowing us to obtain the amount of attenuation in the $H\alpha$ and [OIII] λ 5007 emission lines directly from the fits using photometry and $H\alpha$ emission line fluxes. A comparison to the attenuations estimated with the BD method is addressed in this section.

The reliability of the estimation of the effective attenuation has to be checked carefully. We used a CIGALE option to create and analyze mock catalogs and to verify if the main parameters involved in our derivation can be trusted and ensure that our analysis is robust enough to constrain the attenuation. Each flux in the mock catalog corresponds to the value of the best model and is modified by adding a value taken from a Gaussian distribution centered at 0 and with the same standard deviation as the observations. The mock catalog of fluxes contains the same number of sources and is fitted in the same way as the original catalog. The estimated and exact values for the two free parameters in the [Charlot & Fall \(2000\)](#) recipe and the $H\alpha$ attenuation are compared in Fig. 8. The value for A_V^{ISM} is very well reproduced with a Spearman's correlation coefficient of $\rho_s = 0.95$. The μ parameter is more difficult to constrain even if a clear positive correlation is found between exact and estimated values (Spearman's correlation coefficient of $\rho_s = 0.84$). The ratio of the attenuation in the V-band experienced by the young and old stars characterized by μ is difficult to constrain and as a consequence A_V^{BC} is also not very well constrained. Moreover, $A_{H\alpha}$ is well-constrained with a Spearman's correlation coefficient of $\rho_s = 0.93$, reflecting the effects of the BC+ISM combination.

Attenuation robustness: Mocks, Balmer decrement, and stellar mass trends

The retrieved attenuation for the $H\alpha$ and [OIII] λ 5007 emission lines is a crucial output of the SED fitting process for this work. We can use these values to correct line luminosities as the attenuation is constrained by the energy budget method through the UV-to-IR photometry coverage. Nevertheless, the measure of attenuation based on the BD method is widely used to compute the amount of attenuation when both $H\alpha$ and $H\beta$ are available. Attenuation in the $H\alpha$ line can be obtained directly using the observed $H\alpha$ and $H\beta$ fluxes and assuming a given extinction curve following:

$$A_{H\alpha} = \frac{-2.5\kappa_{H\alpha}}{\kappa_{H\beta} - \kappa_{H\alpha}} \log_{10} \left(\frac{2.86}{H\alpha/H\beta} \right), \quad (5)$$

where $\kappa_{H\alpha}$ and $\kappa_{H\beta}$ represent a particular extinction curve evaluated at $H\alpha$ and $H\beta$ wavelengths, respectively. The attenuation for the hydrogen lines (i.e., $H\alpha$) can be translated into an

Table 3. $H\alpha$ and [OIII] λ 5007 attenuation comparison for selected sample of 80 galaxies. The median values of attenuation and uncertainties are presented. The single-star value is computed using $n^{BC} = -1.3$ instead of -0.7 . The dagger value is obtained including $H\alpha$, $H\beta$, and [OIII] λ 5007 in the fit (see Sect. 6.2).

Method	$A_{H\alpha}$ [mag]	$A_{[OIII]}$ [mag]	$A_{[OIII]} - A_{H\alpha}$
CIGALE fit	1.16 ± 0.19	1.41 ± 0.22	0.25
CIGALE fit*	1.17 ± 0.14	1.53 ± 0.20	0.36
CIGALE fit [†]	1.11 ± 0.18	1.34 ± 0.22	0.23
BD (MW)	0.82 ± 0.19	1.14 ± 0.26	0.31
BD (C00)	0.97 ± 0.22	1.30 ± 0.30	0.33

* with $n^{BC} = -1.3$

[†] including $H\alpha$, $H\beta$, and [OIII] λ 5007 in the fit

attenuation of the [OIII] λ 5007 emission using the same extinction curve at the respective wavelength.

In order to compare BD derived attenuations with CIGALE's attenuation estimates, we selected, from a total of 139 objects with both $H\alpha$ and $H\beta$ measurements, a sub-sample of 80 objects satisfying the $H\alpha/H\beta > 2.86^6$ criterion. Here, 23 of the excluded sources have a Balmer decrement that is consistent with 2.86 within 1σ uncertainty. The rest that are not consistent have over-estimated $H\beta$ fluxes as compared to $H\alpha$. We did not include any of these sources in the analysis so that we could remain consistent with the photoionization models implemented in CIGALE. Excluding values below the canonical value of the ratio allows us to exclude negative attenuation values inconsistent with the case B recombination assumption for the emission lines. We computed the attenuation applying Eq. 5, along with the Milky Way curve ($\kappa_{H\alpha} = 2.52$; and $\kappa_{H\beta} = 3.66$; $\kappa_{[OIII]} = 3.52$) of [Cardelli et al. \(1989\)](#) updated by [O'Donnell \(1994\)](#). For comparison and to show the effects in the derived attenuation due to the choice of an extinction curve, we also considered the [Calzetti et al. \(2000\)](#) (C00) curve ($\kappa_{H\alpha} = 3.33$; and $\kappa_{H\beta} = 4.59$; $\kappa_{[OIII]} = 4.46$)⁷.

In Table 3, we present median attenuation values for $H\alpha$ and [OIII] λ 5007, as well as the $A_{[OIII]} - A_{H\alpha}$ ratio. All values are derived with a fixed BC slope $n^{BC} = -0.7$ except for the starred case in which $n^{BC} = -1.3$ was implemented. The fit with $n^{BC} = -1.3$ is as good as the $n^{BC} = -0.7$ case. In Fig. 9, the derived attenuations using the BD method are compared to CIGALE's estimates. We check the distribution of CIGALE's attenuation in the [OIII] λ 5007 emission line as a function of stellar mass and fit a linear relation shown in orange in the lower panel of Fig. 10. Thus, we obtain:

$$A_{[OIII]} = (1.19 \pm 0.15) + (0.98 \pm 0.22) \log_{10} (M_*/10^{10}M_{\odot}).$$

We go on to explore the effects of using this relation to correct [OIII] λ 5007 luminosities in Sect. 5.3.

Applying either the Milky Way or C00 reddening curve leads to lower median attenuations than those derived using [Charlot & Fall \(2000\)](#) recipe in CIGALE, as shown in Fig. 10. CIGALE's attenuation estimates are globally in agreement with the $A_{H\alpha}$ -mass relation of [Garn & Best \(2010a\)](#). BD derived attenuations

⁶ The intrinsic value of 2.86 is assumed to be consistent with a temperature $T = 10^4$ K and electron density $n_e = 100\text{cm}^{-3}$ for case B recombination [Osterbrock \(1989\)](#) and does not vary significantly with the physical conditions.

⁷ This curve is only valid for stellar continuum and not appropriate to describe nebular emission line attenuation ([Pannella et al. 2015](#); [Reddy et al. 2015](#); [Puglisi et al. 2016](#); [Battisti et al. 2016](#); [Theios et al. 2019](#); [Qin et al. 2019](#); [Shivaei et al. 2020](#)).

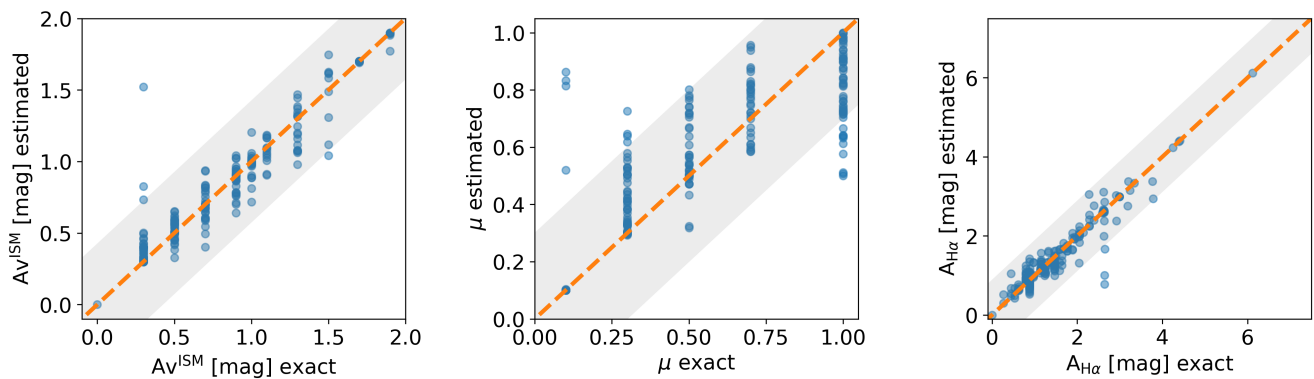


Fig. 8. Mock data sets comparison for the CF00 attenuation recipe intrinsic parameters (A_V^{ISM} and μ), and the $H\alpha$ attenuation. On the y-axis, the estimated values from the mock catalogs are shown. The x-axis corresponds to the exact value retrieved by CIGALE. The dashed line shows the 1:1 relation. The 1σ levels computed as the standard deviation of the estimated parameters are drawn as gray shades.

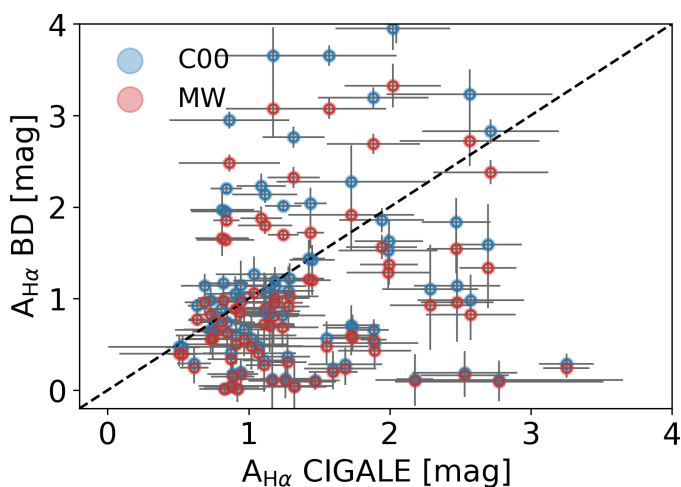


Fig. 9. Balmer Decrement and CIGALE's $A_{H\alpha}$ comparison. Blue and red dots correspond to the BD derived attenuations computed using Eq. 5 and a Calzetti et al. (2000) and Milky Way extinction curve, respectively. The $H\alpha$ attenuation obtained directly from CIGALE is shown in the x-axis. The 1:1 relation is shown as a dashed black line.

(i.e., blue and red dots) are not entirely consistent with this relation placing the majority of the objects below the relation. Objects above Garn & Best (2010a) relation have a SFR $> 10^{1.5} M_{\odot} \text{yr}^{-1}$ but they are not classified as starbursting from our analysis. The $H\alpha$ attenuation increases with stellar mass in agreement with previous works (Garn & Best 2010b,a; Ibar et al. 2013; Zahid et al. 2017; Shivaei et al. 2020), following the Garn & Best (2010a) relation and confirming that in more massive galaxies nebular regions have a higher attenuation (Koyama et al. 2019). This also confirms that this relation is not just valid for the local universe but at higher redshift as well. From the attenuation ratio between [OIII] λ 5007 and $H\alpha$ presented in Table 3, we can see that our results using CF00 lead to a flatter effective attenuation curve (Chevallard & Charlot 2016; Lo Faro et al. 2017; Buat et al. 2018), as compared to the Milky Way or C00 recipe. The difference arises from the choice in fixing both slopes in the CF00 to the same value of -0.7 . We performed the same analysis using $n^{\text{BC}} = -1.3$ and verified that the effective curve is steeper than in the $n^{\text{BC}} = -0.7$ case and closer (and even slightly steeper) than the Milky Way and C00 case.

The attenuation distributions obtained for the entire sample from the SED fitting are shown in Fig. 11 for the $H\alpha$ and

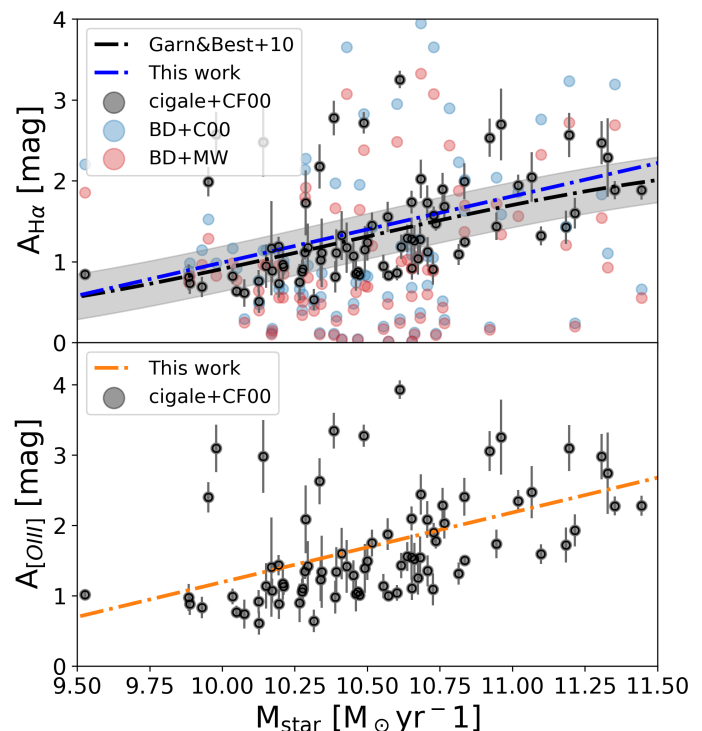


Fig. 10. Variation of the $A_{H\alpha}$, and $A_{[\text{OIII}]}$ attenuation with the stellar mass. The attenuation computed with CIGALE is presented as black dots with their respective uncertainties. Milky Way and C00 are shown in red and blue, respectively without uncertainties for clarity on the upper panel. The dashed line corresponds to the $A_{H\alpha}$ - M_{star} relation obtained by Garn & Best (2010a) in the local universe. The shaded area indicates the relation's $\pm 1\sigma$ distribution width. The blue line represents a linear fit to the black dots. The lower panel corresponds to the attenuation retrieved for the [OIII] λ 5007 emission line. A linear fit is shown in orange.

[OIII] λ 5007 emission lines as well as for the V-band. The nebular line attenuation distribution in both cases follows a similar behavior as both lines are produced inside the HII-regions and they are attenuated in a similar way (inherent to CIGALE modeling). Stellar continuum attenuation as traced by A_V is lower. The differential attenuation suffered by young and old stars is measured by the μ parameter in the CF00 recipe as explained in Sect. 3.3. The original value proposed by Charlot & Fall (2000) corresponds to 0.3 for the nearby universe. We measured a larger

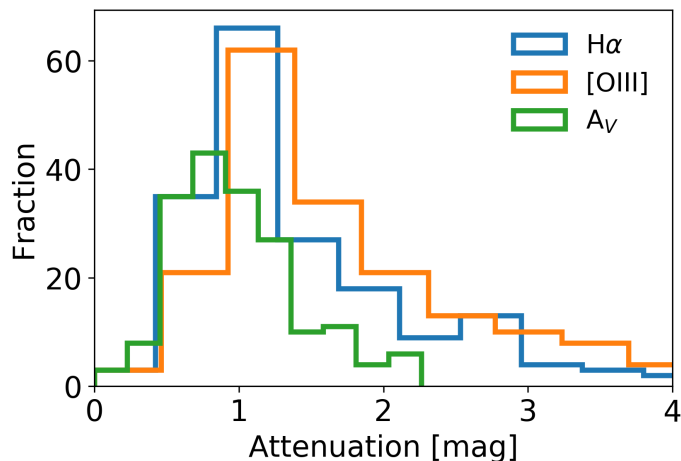


Fig. 11. Distribution of the total attenuation in the $H\alpha$ and $[OIII]\lambda 5007$ emission lines and the V-band are shown in blue, orange, and green, respectively. The amount of attenuation obtained for the emission lines is similar.

value of $\mu = 0.57 \pm 0.14$. In general, higher values are found at higher redshift (see [Buat et al. 2018](#), and references therein). This is in agreement with nebular emission being more attenuated than the stellar continuum.

5. $[OIII]\lambda 5007$, $H\alpha$ fluxes, and SFR measurements

In Sect. 4, we show that we constrain well the attenuation in our sample with the multi-wavelength plus IR bands coverage and the inclusion of the $H\alpha$ emission line, and the CF00 recipe, which introduces a differential attenuation between young and old stellar populations.

We computed the $[OIII]\lambda 5007$ line luminosities for our sample of galaxies using FMOS-COSMOS observed fluxes. These luminosities are corrected for dust effects using the Bayesian attenuation $A_{[OIII]}$ presented in Sect. 4. We find that the $H\alpha$ and $[OIII]\lambda 5007$ emission lines span a similar range in luminosities and the amount of attenuation is found to increase with luminosity and SFR confirming previous works (e.g., [Cortese et al. 2012](#); [Bourne et al. 2012](#); [Santini et al. 2014](#)). In Fig. 12, the observed and dust corrected $H\alpha$ and $[OIII]\lambda 5007$ luminosities are shown in gray and color dots, respectively. Emission lines are not strongly correlated before dust correction. After accounting for dust attenuation both quantities correlate (with a Spearman’s coefficient of $\rho_s = 0.6$). In the next subsections, we address the gas-phase metallicity influence on the $[OIII]\lambda 5007/H\alpha$ line ratio, the SFR measurements, and we compare both $[OIII]\lambda 5007$ and $[OIII] 88 \mu\text{m}$ line emissions from the photoionization models.

5.1. Gas-phase metallicity

The $[OIII]\lambda 5007$ emission line is sensitive to the ionization parameter (i.e., the ionizing field; [Kewley et al. 2013](#); [Kewley et al. 2013](#); [Dopita et al. 2013, 2016](#); [Nicholls et al. 2017](#)) but can be also affected by the gas-phase metallicity ([Kennicutt 1992](#); [Kennicutt et al. 2000](#); [Steidel et al. 2014](#); [Gutkin et al. 2016](#); [Byler et al. 2017](#)). Different mass metallicity relations (MZR) based on direct and strong-line methods are reported in literature, sometimes including the effects of the SFR (e.g., [Pettini & Pagel 2004](#); [Mannucci et al. 2010](#); [Andrews & Martini 2013](#); [Zahid et al. 2017](#); [Sanders et al. 2021, 2020](#); [Curti et al.](#)

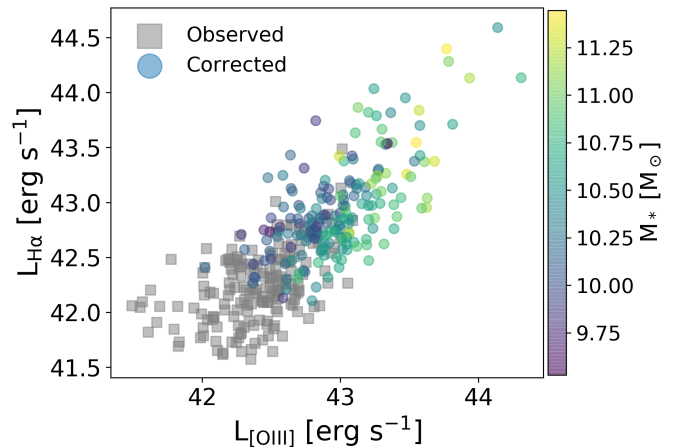


Fig. 12. $H\alpha$ and $[OIII]\lambda 5007$ luminosity. The observed luminosities uncorrected for dust are shown as gray dots. The color dots correspond to luminosities de-reddened using $A_{H\alpha}$ and $A_{[OIII]}$ as constrained by the SED fitting with CIGALE. The corrected data is color-coded by the stellar mass. A slope of 0.99 is measured in the dust corrected sample with a 0.39 dex dispersion.

[2020](#)). We compute oxygen abundances using the fundamental metallicity relation (FMR) calibration of [Curti et al. \(2020\)](#), which is based on strong-line oxygen abundance measurements for Sloan Digital Sky Survey (SDSS) galaxies. Their relation is fully consistent with a relation derived for a MOSFIRE Deep Evolution Field (MOSDEF) sample of individual and stacked galaxies at $z \sim 2.3$ in [Sanders et al. \(2021\)](#). The dust-corrected $[OIII]\lambda 5007/H\alpha$ ratio is presented in Fig. 13 as a function of oxygen abundance. Our galaxy sample covers a sub-solar abundance range of $8.4 < 12 + \log(O/H) < 8.8$ (i.e., gas-phase metallicity $0.006 < Z_{\text{gas}} < 0.016$)⁸. The ratio slightly decreases when metallicity increases. The median value of the ratio is 0.86 (or -0.065 dex) with a dispersion of 0.3 dex as measured by the standard deviation of the data set. The dispersion at a fixed metallicity can be produced by the sensitivity of the oxygen species to the ionizing field. The dependence on both metallicity and ionizing field is likely to produce effects on the ratio which we cannot easily disentangle. In Sect. 6.2, we explore variations of the intensity of the radiation field fixing the gas-phase metallicity in three bins with an equal number of galaxies and simultaneously fitting the $H\alpha$, $H\beta$, and $[OIII]\lambda 5007$ line fluxes.

5.2. SFR– $[OIII]\lambda 5007$ calibration

In Fig. 14, we present the dust-corrected $[OIII]\lambda 5007$ observed luminosities, and SED fitting derived SFR. As we want to make a comparison with the relations in the literature based on a fixed $[OIII]\lambda 5007/H\alpha$ ratio, we first fit only the intercept using an orthogonal distance regression (ODR) in the $L_{[OIII]}$ -SFR plane. The quality of the fit is measured by the non-parametric Spearman’s and Kendall’s correlation coefficients equal to $\rho_s = 0.57$ and $\rho_s = 0.40$, respectively. This leads to:

$$\log_{10} \text{SFR} = \log_{10} L_{[OIII]} - (41.27 \pm 0.03),$$

with the luminosity and SFR expressed in units of ergs s^{-1} and $M_{\odot} \text{ yr}^{-1}$, respectively.

The presence of outliers can have an impact on the ODR fit. To reduce the effects of extreme values we compute the geomet-

⁸ The solar metallicity is $z_{\odot} = 0.0142$ as in [Grevesse et al. \(2010\)](#).

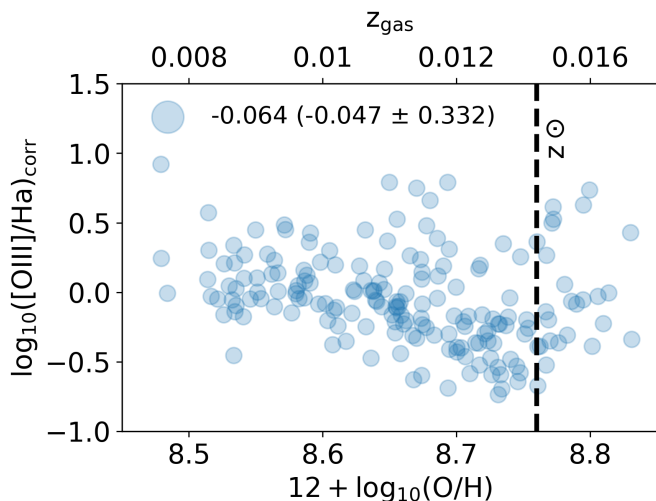


Fig. 13. [OIII] λ 5007/ $H\alpha$ ratio corrected for dust attenuation. We present the logarithm of the ratio as a function of oxygen abundance computed using Curti et al. (2020) FMR relation on the x-axis. The secondary axis corresponds to the translation in terms of gas-phase metallicity where the solar values are 0.0142 or 8.76. The ratio has been corrected using the attenuation for each line as computed with CIGALE. A linear and logarithmic median and mean ratio of 0.86 (-0.065) and 0.89 (-0.047) are found. The 0.32 dispersion corresponds to the standard deviation.

rical distance of each data point to the line drawn by the equation above. We check the geometrical distance distribution and trim 15 data points with $d \geq \pm 0.45$ that corresponds to $\sim 2\sigma$. These outliers are characterized by poor S/N in GALEX NUV, and the *Herschel* bands. We check that the distribution in the SFR- $L_{[\text{OIII}]\lambda 5007}$ plane after discarding these points remains representative of our sample. We implemented a bootstrap method that uses a random iterative replacement technique to estimate the slope and intercept in the fits. Using this method, we drew a new sample of the same size 200 times and re-fit using the ODR method with a fixed slope to obtain the distribution of the intercept from which we compute the mean value and the uncertainty in the intercept as the standard deviation of the distribution. This leads to:

$$\log_{10} \text{SFR} = \log_{10} L_{[\text{OIII}]} - (41.20 \pm 0.02), \quad (6)$$

with the luminosity in ergs s^{-1} and SFR in $M_{\odot} \text{ yr}^{-1}$. The relation is consistent within a 2σ uncertainty with the equation obtained including the outliers. Following the same procedure described earlier in this paper and allowing the slope and intercept to vary, we obtain:

$$\log_{10} \text{SFR} = (0.83 \pm 0.06) \log_{10} L_{[\text{OIII}]} - (34.01 \pm 2.63), \quad (7)$$

with the luminosity and SFR given in units similar to Eq. 6. The slope in Eq. 7 is consistent with unity at 3σ . The relations presented in Eq. 6 and 7 are drawn in Fig. 14 as a black dashed and continuous line with a 0.32 dex dispersion from the standard deviation of the observations as a gray shaded area. Since the $H\alpha$ emission can be considered as proportional to the SFR, the dispersion of the [OIII] λ 5007-SFR correlation is expected to have the same origin as the one affecting the [OIII] λ 5007/ $H\alpha$ ratio: the metallicity and radiation field.

Several authors in the past studied the link between the [OIII] λ 5007 emission line and SFR based on a fixed

[OIII] λ 5007/ $H\alpha$ ratio and the calibration of the $H\alpha$ emission line in terms of SFR. At $z \sim 0.1$ on a sample of 196 SDSS narrow band emitters Moustakas et al. (2006) measured a scatter in the [OIII] λ 5007-SFR relation as large as a factor of 3 – 4 uncertainty (1σ) when compared to other tracers such as [OII] λ 3727, $H\beta$ emission lines or the U-band. Based on a sample of 92 galaxies at $0.40 < z < 0.64$, Hippelein et al. (2003) derived an [OIII] λ 5007/ $H\alpha$ ratio of 0.79 from line luminosity functions, which is consistent with our median value. Although [OIII] λ 5007 depends on excitation and metallicity, their estimated median values of SFR([OIII]) were consistent with the evolution of SFR density of the universe. Ly et al. (2007) reported a [OIII] λ 5007/ $H\alpha$ ratio of 1.05 at $z = 0.07 - 1.47$ for a spectroscopic sample of 196 narrow-band emitters. Teplitz et al. (2000) fixed the ratio to unity at $z > 3$ for a sample of five galaxies observed with the near-IR camera on the Keck I telescope. Both works from Teplitz et al. (2000) and Ly et al. (2007) found similar results on the dependence of the line ratio on metallicity and ionization field. Maschietto et al. (2008) studied a sample of 13 [OIII] emitters at $z \sim 3.09 - 3.16$ and using a [OIII] λ 5007/ $H\alpha$ ratio of 2.4 derived a lower limit relation for SFR and [OIII] λ 5007 luminosity. Straughn et al. (2009) also explored the relation based on [OIII] λ 5007/ $H\alpha$ ratios in knots of 136 galaxies at $z \sim 0.5$ for which both emission lines were observed. Their relation implies a median [OIII] λ 5007/ $H\alpha$ ratio of ~ 1.23 . Bowman et al. (2019) found a strong correlation but did not propose any relation for a set of 3D-HST galaxies at $z \sim 2$ (see their Figure 6).

Our calibration relies on quantities estimated for each galaxy (e.g., [OIII] λ 5007 luminosity, SFR). It can be compared to relations also obtained with individual [OIII] λ 5007/ $H\alpha$ ratios as those obtained by Hippelein et al. (2003), and Ly et al. (2007)⁹. Their dust corrected relations are reported in Fig. 14 (orange and green lines) and are fully consistent with our result within the 1σ dispersion error and our median reported [OIII] λ 5007/ $H\alpha$ ratio of 0.86.

5.3. Impact of the [OIII] λ 5007 dust attenuation

In the previous section, we studied the relation between the [OIII] λ 5007 dust corrected luminosity and SFR. In practice, it is very difficult to correct the [OIII] λ 5007 emission line for dust attenuation. When $A_{[\text{OIII}]}$ cannot be estimated but stellar masses are known, attenuations can be tentatively estimated by using the $A_{[\text{OIII}]}-M_{\text{star}}$ relation presented in Sect. 4. We applied this relation to correct our observed [OIII] λ 5007 luminosities and checked how the relation presented in Eq. 6 is modified. Following the same procedure presented in Sect. 5.2, we find:

$$\log_{10} \text{SFR} = \log_{10} L_{[\text{OIII}]} - (41.23 \pm 0.03). \quad (8)$$

The average relation is similar to that of Eq. 6, but a large dispersion is expected because of the dispersion in the $A_{[\text{OIII}]}-M_{\text{star}}$ relation. To test it, we divided our sample in mass bins of 0.5 dex from $10^{9.5}$ to $10^{11.5} M_{\odot}$ and applied both CIGALE's estimated attenuation and the mass-method attenuation. We measured an average increase in SFR of only 0.15 dex when we apply Eq. 8, as compared to the SFR estimated by CIGALE. The dispersion of 0.3 dex in each bin is much larger than the increase in SFR. Thus, Eq. 8 can be applied when only an averaged value of SFR is needed when analyzing galaxies whose stellar masses are known.

⁹ All relations are converted to Chabrier IMF

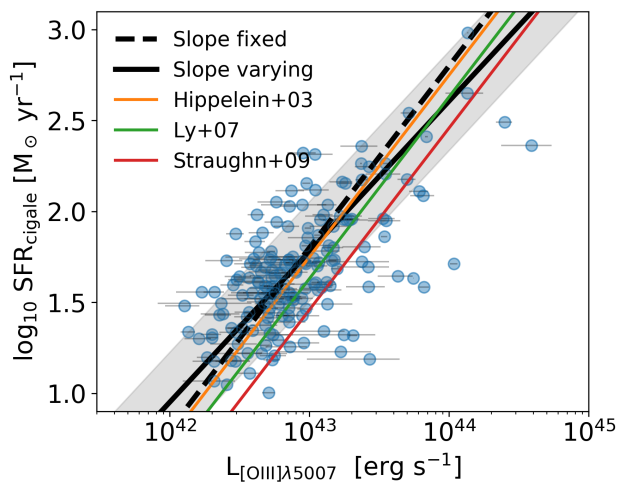


Fig. 14. [OIII] λ 5007 corrected luminosity and SFR relation. The dashed and continuous black lines correspond to fits using a bootstrapped orthogonal distance regression method with a Spearman’s regression coefficient $\rho_s = 0.57$. The 0.32 dex dispersion from the standard deviation is presented as a gray shaded area. The relation shows a positive correlation with scatter significantly higher compared to Kennicutt (1998) H α relation. Relations proposed by Hippelein et al. (2003), and Ly et al. (2007) are shown in orange and green, respectively. Straughn et al. (2009) is also presented in red for comparison. Relations are converted from Salpeter to Chabrier IMF.

5.4. Benchmark for the [OIII] λ 5007 and [OIII] 88 μ m lines

The [OIII] also produces a fine-structure emission line at 88.33 μ m from low excitation and highly ionized gas located in a low-density environment. This line is not affected by dust attenuation and is also used to trace SFR at both low and high redshifts (e.g., De Looze et al. 2014; Harikane et al. 2020). In this section, we present our efforts to predict a relation between [OIII] 88 μ m and SFR from the relation we measured between [OIII] λ 5007 and SFR and HII-region models.

The [OIII] λ 5007-[OIII] 88 μ m ratio is known to vary with gas-phase metallicity and density (Dinerstein 1983; Stacey et al. 2010; Ferkinhoff et al. 2010; Moriwaki et al. 2018), but it is not considered to be especially sensitive to the ionization parameter (Moriwaki et al. 2018). To select the photoionization models that are relevant to our analysis, we restricted the ionization parameter to $-3.0 < \log U < -2.0$, in agreement with our results (presented in Sect. 6.2). For the electron density, Kashino et al. (2017) derived a value of $\sim 200 \text{ cm}^{-3}$ for the FMOS-COSMOS sample. Three different values of the electron density are available in CIGALE (i.e., $n_e = 10, 100, \text{ and } 1000 \text{ cm}^{-3}$) and we fixed n_e to 100 cm^{-3} . From our estimations of the gas-phase metallicity (Sect. 5.1), we restricted the models to $0.006 < Z_{\text{gas}} < 0.016$ (or $8.4 < 12 + \log(\text{O}/\text{H}) < 8.8$). With the selected models, we derived a mean [OIII] λ 5007-[OIII] 88 μ m ratio of ~ 1.90 (with a 1σ dispersion of 0.84). We used this average value of the ratio to translate our SFR-[OIII] λ 5007 linear relation (presented in Eq. 6) into another linear relation between [OIII] 88 μ m and SFR. This is presented in Fig. 15 as a black dotted line with a gray shaded area accounting for the dispersion with the gas-phase metallicity.

Our relation is found to be consistent with the relations proposed by De Looze et al. (2014) for metal-poor local dwarf galaxies and by Harikane et al. (2020) for high redshift galaxies despite the different gas-phase metallicities of their samples. Arata et al. (2020) report a $L_{[\text{OIII}]88\mu\text{m}} - \text{SFR}$ relation derived

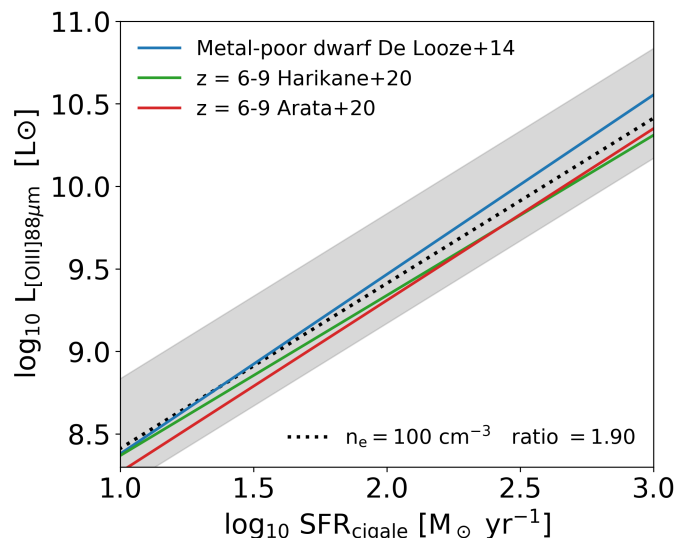


Fig. 15. [OIII] 88 μ m-SFR relation. The blue line shows the metal-poor local dwarf galaxies relation from De Looze et al. (2014). The green line corresponds to the high-redshift observed relation proposed by Harikane et al. (2020) while the red line corresponds to simulation results from Arata et al. (2020) both at $z = 6 - 9$. We translate our [OIII] λ 5007 luminosities into [OIII] 88 μ m using a mean ratio of 1.9 derived from CLOUDY HII-region models at an electron density of $n_e = 100 \text{ cm}^{-3}$ shown as a black dotted line. The gray area is the dispersion in the translation with gas-phase metallicity.

from simulations at $z = 6 - 9$ covering a gas-phase metallicity range of $6.6 < 12 + \log(\text{O}/\text{H}) < 8.9$ that matches our metallicity range and is also consistent with different predictions from the literature (De Looze et al. 2014; Moriwaki et al. 2018; Harikane et al. 2020). Both electron density and gas-phase metallicity are paramount to properly convert one emission into the other as well as to compare different samples of galaxies. At intermediate and high densities [OIII] λ 5007 line remains an important coolant for ionized gas as compared to [OIII] 88 μ m. The [OIII] λ 5007 emission line will be targeted in future surveys like MOONS, PFS, and JWST allowing for synergies with observatories like ALMA that can perform observations of [OIII] 88 μ m at high-redshift providing a direct method to characterize the overall cooling budget and the ISM physics of HII-regions in intermediate- and high-redshift galaxies as well as to refine their calibration in SFR.

6. Spectro-photometric modeling: HII-region and stellar continuum modeling

Our FMOS-COSMOS sample has H α , H β , [NII] λ 6584, [OIII] λ 5007, [SII] λ 6717, and [SII] λ 6731 fluxes (c.f Sect. 2). In our initial SED fitting analysis, we only included the H α emission line because of the current challenges in the production of the photoionization models to reproduce observations. We discuss these issues in this section and introduce more line intensities to the fits.

The nebular emission lines module was briefly introduced in Sect. 3.2; here, we add a more detailed description of the photoionization calculations. We use the CLOUDY 17.01 photoionization code (Ferland et al. 2017) to predict the relative intensities of 124 atomic lines originating from the far-ultraviolet (FUV) to FIR. Line emissivity models for a plane-parallel geometry are built with the intensity of the photo-ionizing radiation

Table 4. Connection between the stellar and gas-phase metallicity.

Z_{star}	Z_{gas}
0.05	0.051, 0.046, 0.041
0.02	0.037, 0.033, 0.030, 0.025, 0.022, 0.019, 0.016, 0.014
0.008	0.012, 0.011, 0.009, 0.008, 0.007
0.004	0.006, 0.005, 0.004, 0.003
0.0004	0.0025, 0.002, 0.001, 0.0004
0.0001	0.0001

field varying from $-4.0 < \log U < -1.0$ and using a sampling of 0.1 dex. The electron density is set to three different values of $n_e = 10, 100, 1000 \text{ cm}^{-3}$ covering 25 gas-phase metallicities spanning over $0.0001 < Z_{\text{gas}} < 0.05$ disconnected from stellar metallicity (0.0001, 0.0004, 0.004, 0.008, 0.02, 0.05) as presented in Table 4. The closest stellar metallicity to the gas-phase metallicity is chosen as the input ionizing spectrum in the models. The cosmic abundance standard and the derivation of element abundances implemented in our models are discussed in Nicholls et al. (2017). They are based on a scaling developed by Nieva & Przybilla (2012) derived from observed metallicities of 29 early B-type stars in the Milky Way. The depletion onto grains is not taken into account since the abundances are based on gas-phase measurements. Our models are built on the so-called local Galactic concordance, $12 + \log(\text{O}/\text{H})_{\text{GC}} = 8.76$, which is close to the 8.73 estimated primordial solar abundance derived by Asplund et al. (2009) and Lodders (2010), with $(\text{O}/\text{H})_{\text{GC}} = 5.76 \times 10^{-4}$, $(\text{N}/\text{H})_{\text{GC}} = 6.17 \times 10^{-5}$, $(\text{C}/\text{O})_{\text{GC}} = 0.46$, and $Z_{\text{GC}} = 0.0142$. Super-solar and sub-solar metallicities are scaled following the latter definitions. As compared to the previous version implemented in CIGALE, these models disconnect the stellar and gas-phase metallicities and implement current abundance measurements, making them more appropriate for reproducing the line fluxes of our sample of galaxies. We used these new models to fit both photometry and other emission lines similar to Sect. 5, where photometry and only $\text{H}\alpha$ emission fluxes were fitted together.

6.1. Baldwin-Phillips-Terlevich and [SII] $\lambda\lambda$ 717,31 excitation diagrams

In Fig. 16, the [OIII] λ 5007/ $\text{H}\beta$, [NII] λ 6584/ $\text{H}\alpha$ diagram (so-called Baldwin-Phillips-Terlevich (Baldwin et al. 1981); see also Veilleux & Osterbrock (1987)) and the [SII] $\lambda\lambda$ 6717,31 excitation diagrams (hereafter [NII]-BPT and [SII]-BPT) along with our photoionization models are presented color-coded by the ionization parameter and the gas-phase metallicity. In the left panel, the demarcation between star-forming galaxies and systems hosting an AGN of Kauffmann et al. (2003) from SDSS data at $z = 0$ is shown as a black thick line and the extreme starburst separation line of Kewley et al. (2013) at $z = 1.6$ as a dashed line. The blue, green, and orange lines correspond to best-fit relations for the loci of galaxies in the [NII]-BPT at $z \sim 2.2$, $z \sim 2.3$, and $z \sim 1.6$ from Strom et al. (2017), Shapley et al. (2015), and Kashino et al. (2017), respectively. Individual FMOS-COSMOS points show the well-known offset from the local sequence. Our FMOS-COSMOS sample with valid measurements for the four emission lines and their corresponding measured errors are represented by dots. For a smaller sample of 16 objects, we show, in the right panel, the [SII]-BPT diagram with the star-forming and AGN separation of Kewley et al. (2001) and the best fit for the loci of galaxies of Strom et al. (2017).

The CLOUDY models cover well the star-forming region below the Kauffmann et al. (2003) line in the [NII]-BPT diagram. However, only 61% of the flux ratios presented are covered pointing toward a difficulty related to the nitrogen-to-oxygen abundances more than the photoionizing field. In this diagram, 23% of the objects lie in the composite region where AGN and star-forming galaxies coexist at $z = 0$. For the [SII]-BPT diagram models are in agreement with the locus of galaxies with valid measurements within the observational errors. The HII-region models able to predict emission line ratios above the local star-forming relation are difficult to create because of *i.* nitrogen abundance underestimation; *ii.* ionizing field hardness choice; *iii.* gas-phase metallicity and density discrepancies or single stellar population models. The models depend strongly on the relative abundances of nitrogen and oxygen, and thus on the choice of the standard metallicity scale (e.g., Nicholls et al. 2017). The nebular scaling of nitrogen with oxygen is problematic: while oxygen is principally produced in core-collapse supernovae in the native gas cloud from which the HII-region formed, nitrogen has both primary and secondary abundances, which are caused by delayed nucleosynthesis through hot-bottom burning and dredge-up in intermediate-mass stars as they evolve (Vila-Costas & Edmunds 1993). Increasing the nitrogen abundance has been suggested by many authors as a way to match the observations (e.g., Masters et al. 2014, 2016; Steidel et al. 2014; Shapley et al. 2015; Yabe et al. 2015; Cowie et al. 2016; Sanders et al. 2016). A shift by 0.2 – 0.4 dex in the N/O fraction is proposed by Masters et al. (2016) while Kojima et al. (2017) and Strom et al. (2017) require ~ 0.1 dex to cover the locus of galaxies in the BPT at $z \sim 2.3$. We find that in order to cover all the sample of galaxies at $z \sim 1.6$, a shift of 0.2 – 0.3 dex is necessary. [OIII] λ 5007 and [NII] λ 6584 have an ionization potential (IP) of 35.12 and 14.53 eV and are ionized by both charge transfer with protons and photoionization. Thus, [OIII] λ 5007 and [NII] λ 6584 abundances are less sensitive to the photoionizing field, which are determined indirectly through the HII abundance, and the initial oxygen and nitrogen abundances. [SII] $\lambda\lambda$ 6717, 37 has an IP of 10.36 eV, making its abundance very sensitive to the hardness of the photoionizing field in the UV. Indeed, Steidel et al. (2014, 2016) applied harder radiation fields using the binary Population and Spectral Synthesis code (BPASS) and these authors were able to produce models covering larger values of $\log([\text{OIII}]\lambda 5007/\text{H}\beta)$, but always below the Kauffmann et al. (2003) line. Other authors point to a higher ionization parameter or electron density as the main parameter producing the offset (e.g., Brinchmann et al. 2008; Kewley et al. 2013; Kewley et al. 2013; Dopita et al. 2016; Kojima et al. 2017; Bian et al. 2020). Nevertheless, current stellar synthesis models are unable to produce such hard radiation fields (Levesque et al. 2010). The densities from models in high-redshift galaxies ($z \geq 1 - 2$) are higher than in low-redshift galaxies, on the order of several 10^2 to several 10^3 per cm^{-3} (Shimakawa et al. 2015; Kashino et al. 2017). Density (i.e., the pressure) has only secondary effects on the locus of the models in the [NII]-BPT diagram (Masters et al. 2016).

6.2. $\text{H}\alpha$ $\text{H}\beta$ and [OIII] λ 007 SED fitting

To test the performance of SED fitting including more emission lines, we fit simultaneously the photometry and the $\text{H}\alpha$, $\text{H}\beta$, and [OIII] λ 5007 fluxes to explore the impact of the ionization parameter in the dispersion of the proposed $\text{SFR-L}_{[\text{OIII}]}$ relation. Our sample of galaxies spans over a gas-phase metallicity range of $0.006 < Z_{\text{gas}} < 0.016$ (see Sect. 5). We di-

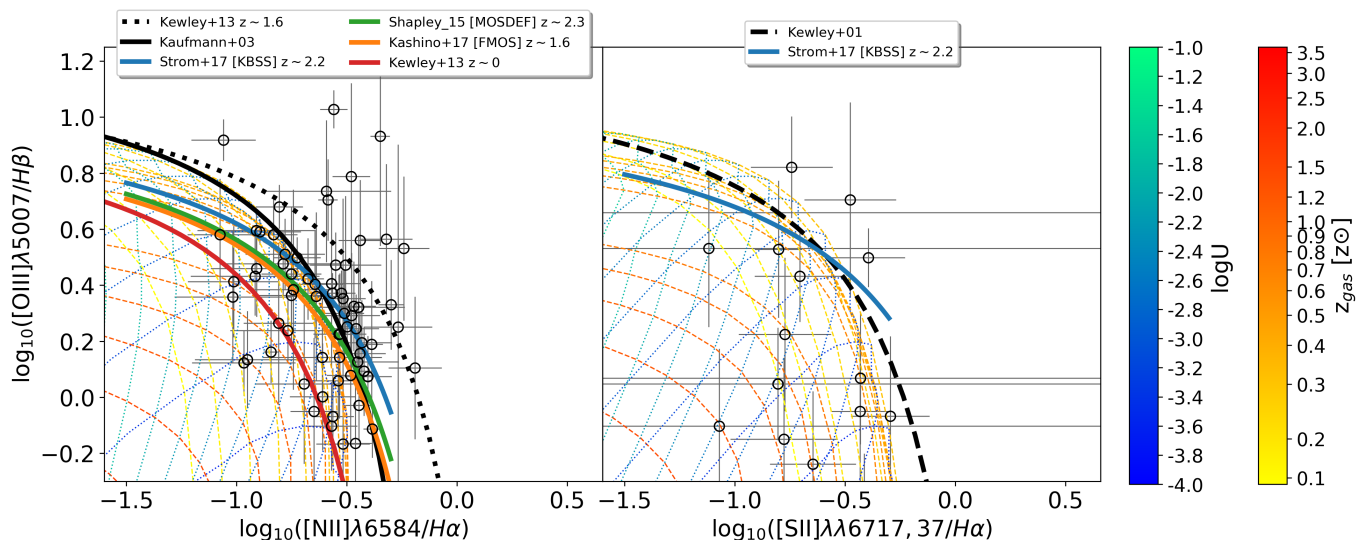


Fig. 16. Excitation diagnostic diagrams. **Left:** Baldwin–Phillips–Terlevich (BPT) diagram ($[\text{OIII}]\lambda 5007/\text{H}\beta$ versus $[\text{NII}]\lambda 6584/\text{H}\alpha$). The new models implemented in CIGALE are color-coded by gas-phase metallicity in solar units and ionization parameter $\log U$. Only a few metallicities are shown for clarity. The FMOS-COSMOS sample is shown as gray dots with error bars. The solid black line corresponds to the [Kauffmann et al. \(2003\)](#) relation and the dashed-black line corresponds to [Kewley et al. \(2013\)](#) evaluated at $z \sim 1.6$. The curves of [Shapley et al. \(2015\)](#), [Kashino et al. \(2017\)](#), and [Strom et al. \(2017\)](#) are shown in green, orange, and blue, respectively. The red line represents the local-universe locus of galaxies as shown by [Kewley et al. \(2013\)](#). **Right:** $[\text{SII}]\lambda\lambda 6717,31$ excitation diagram ($[\text{OIII}]\lambda 5007/\text{H}\beta$ versus $[\text{SII}]\lambda\lambda 6717,31/\text{H}\alpha$). The current models implemented in CIGALE are color-coded by gas-phase metallicity and ionization parameter $\log U$ to illustrate the coverage. Only a few metallicities are shown for clarity. The FMOS-COSMOS sample is shown as black circles with error bars. The dashed black line corresponds to the results from [Kewley et al. \(2001\)](#) and the blue line to [Strom et al. \(2017\)](#).

vide the sample in three different gas-phase metallicity bins with roughly equal number of sources and median metallicities given by $Z_{\text{gas}} = 0.009$, $Z_{\text{gas}} = 0.011$ and $Z_{\text{gas}} = 0.014$. We perform SED fitting including the UV-to-FIR photometry and the $\text{H}\alpha$, $\text{H}\beta$, and $[\text{OIII}]\lambda 5007$ emission lines by fixing the gas-phase metallicity in each bin to its median value. Only two stellar metallicities of the BC03 models, 0.02 and 0.008, are included in the full range of gas-phase metallicity of our sample. We set the stellar metallicity to 0.02 after checking that using 0.008 does not affect our parameter estimation. In the case of $\text{H}\beta$ we only include measurements of the lines for objects satisfying $\text{BD} > 2.86$ to be consistent with our models. We let the ionization parameter to vary between $-4.0 < \log U < -1.0$ and we use $n_e = 100 \text{ cm}^{-3}$ consistent with the electron density derived by [Kashino et al. \(2017\)](#) for the FMOS-COSMOS sample.

We exclude from the analysis 21 objects with a difference between observed and fitted fluxes larger than 0.2 dex for the three emission lines. In Fig. 17 the observed and estimated fluxes from the three emission lines are compared. In the case of the $\text{H}\alpha$ line as compared to our previous fit in Fig. 6 similar results are obtained and the line fit is not improved by including more emission lines. The distribution of the estimated $[\text{OIII}]\lambda 5007$ fluxes is not symmetric with an excess of overestimated fluxes. $\text{H}\beta$ estimated fluxes have a standard deviation of ~ 0.13 dex which is twice as large as that of $\text{H}\alpha$ and $[\text{OIII}]\lambda 5007$ emission lines. We obtain a median attenuation from CIGALE of $A_{\text{H}\alpha} = 1.11 \pm 0.18$ mag and $A_{[\text{OIII}]} = 1.34 \pm 0.22$ mag (\dagger as reported in Table 3), consistent with values derived using photometry and the $\text{H}\alpha$ emission only. Stellar mass, SFR, and attenuation in the $\text{H}\alpha$ and $[\text{OIII}]\lambda 5007$ emission lines are not found to vary significantly by including more emission lines in the SED fitting process as shown in Fig. 18.

Using mock catalogs created with CIGALE we investigate the robustness in the estimation of the ionization parameter

$\log U$. The exact and estimated values of $\log U$ are compared in the bottom-right panel in Fig. 17 showing a good agreement within a 0.6 dex (1σ) dispersion for the three different gas-phase metallicity bins guaranteeing the reliability in the estimation of the ionization parameter.

From our fit, we estimate median values of $\log U_{0.009} \sim -2.74$, $\log U_{0.011} \sim -3.03$, and $\log U_{0.014} \sim -2.79$, while including the $\text{H}\beta$, and $[\text{OIII}]\lambda 5007$ lines. The 16th and 84th percentiles in $\log U$ for each gas-phase metallicity bin are $\log U_{0.009} \sim -3.02, -2.35$, $\log U_{0.011} \sim -3.21, -2.60$, and $\log U_{0.014} \sim -3.14, -2.00$, respectively. [Kaasinen et al. \(2018\)](#) measured $\log U \sim -2.72$ from an evolutionary analysis of the ionization parameter using a sample of 50 star-forming galaxies selected from the FMOS-COSMOS catalog with DEep Imaging Multi-Object Spectrograph (DEIMOS) observations. [Sanders et al. \(2020\)](#) constrain the ionization parameter using BPASS grids for a MOSDEF and Keck Baryonic Structure Survey (KBSS) samples at $z \sim 1 - 3$ to $\log U \sim -2.63$ and $\log U \sim -2.85$, respectively. [Topping et al. \(2020\)](#) found that the local $12 + \log(\text{O}/\text{H}) - \log U$ relationship of [Pérez-Montero \(2014\)](#) for low-redshift galaxies is still applicable at $z \sim 2$. From this relation, the ionization parameter range for our sample should span over the range $-3.2 < \log U < -2.5$, in agreement with our estimations.

The $\text{SFR} - L_{[\text{OIII}]\lambda 5007}$ ratio can be interpreted as the $\text{H}\alpha - [\text{OIII}]\lambda 5007$ ratio because $\text{H}\alpha$ is a tracer of SFR. The dispersion in the $[\text{OIII}]\lambda 5007/\text{H}\alpha$ dust corrected ratio (Fig. 13) depends on both ionization parameter and gas-phase metallicity. Now we explore the influence of the ionization parameter on our previous relation between the SFR and $[\text{OIII}]\lambda 5007$ (Sect. 5). In Fig. 19, we present $\text{SFR}/L_{[\text{OIII}]\lambda 5007}$ from Eq. 6 as a function of the ionization parameter that we derived from the fit with emission lines and the three different median metallicities in each bin. In this figure, the error bar symbols represent the median values for each bin of gas-phase metallicity with the

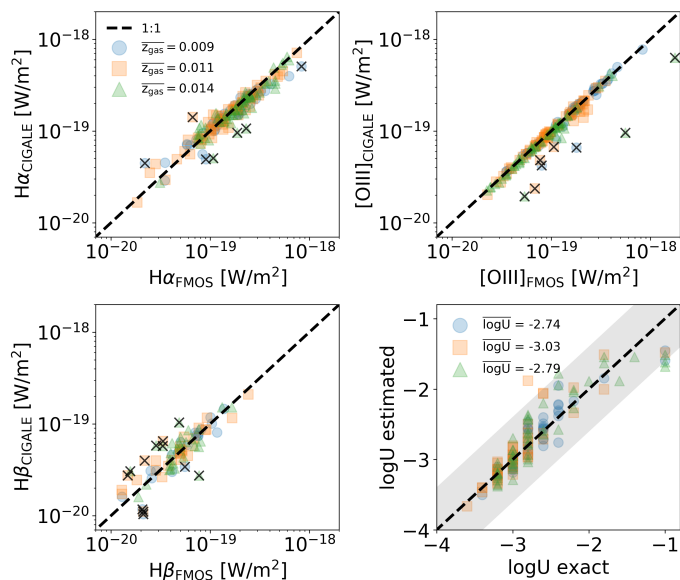


Fig. 17. Quality of the fits including $H\alpha$, $H\beta$, and [OIII] λ 5007 emission lines and ionization parameter estimation. From left to right, top to bottom, we show the CIGALE fit vs. observed flux for the $H\alpha$, [OIII] λ 5007, $H\beta$ emission lines. The three different gas-phase metallicity bins are presented as blue circles, orange squares, and green triangles. The black crosses correspond to excluded data with flux difference larger than 0.2 dex. The black line corresponds to the 1:1 relation. The three emission lines are well fitted for the three different median gas-phase metallicity models. The last panel shows the estimated vs exact value for $\log U$ from mock samples created with CIGALE. Symbols are the same as the legend in the first panel and the median ionization parameter value is shown. The shaded area corresponds to the standard deviation.

standard deviation as the error. We measured median ratios of $([OIII]\lambda 5007/H\alpha)_{0.009} = 1.12$, $([OIII]\lambda 5007/H\alpha)_{0.011} = 0.79$ and $([OIII]\lambda 5007/H\alpha)_{0.014} = 0.54$ in each gas-phase metallicity bin. However similar average $\log U$ values can lead to different [OIII]/ $H\alpha$ ratios due to variations with gas-phase metallicity. In Table 5, we show median values of the $SFR-L_{[OIII]\lambda 5007}$ ratio for each gas-phase metallicity in 0.5 dex $\log U$ bins for the $-3.5 < \log U < -2.5$ range in which the ratio seems to be quite stable. We measure a mean dispersion of 0.24 dex in gas-phase metallicity and 1.1 dex for the ionization parameter in the range $-3.5 < \log U < -2.5$. The effects of the ionization parameter on the $SFR-L_{[OIII]\lambda 5007}$ dispersion are dominant, but our sample covers only a range of 0.4 dex in the gas-phase metallicity. A sample spanning over a larger range of metallicity is needed to explore in detail the relative influence of both parameters. Our results are consistent with previous studies (e.g., Pérez-Montero 2014; Kaasinen et al. 2018; Sanders et al. 2020; Topping et al. 2020).

In a future work, we plan to explore the effects of using SED fitting with CIGALE implementing BPASS to explore how the locus of galaxies in the [NII]-BPT is affected, leaving the abundance ratio of (N/O) as a free parameter to introduce flexibility in HII-region models and checking also different ways of modeling the emission lines. The SED fitting and HII-region model coupling remains paramount in order to perform homogeneous analysis of a sample of galaxies and break degeneracies between the different parameters involved. Fully understanding of working with spectro-photometric samples and SED fitting is needed as a preparation for new instruments such as PFS and MOONS.

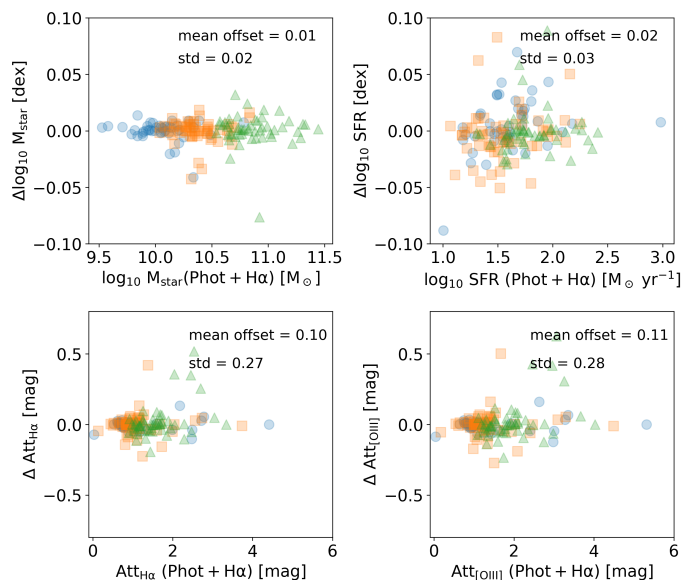


Fig. 18. Stellar mass, SFR, and $H\alpha$ and [OIII] λ 5007 attenuation. We compare the derived parameters using photometry and $H\alpha$ flux in the SED fitting and adding $H\beta$ and [OIII] λ 5007 fluxes. The three different gas-phase metallicity bins are presented as blue circles, orange squares, and green triangles as in Fig. 17. The mean offset and dispersion of the are shown for each parameter.

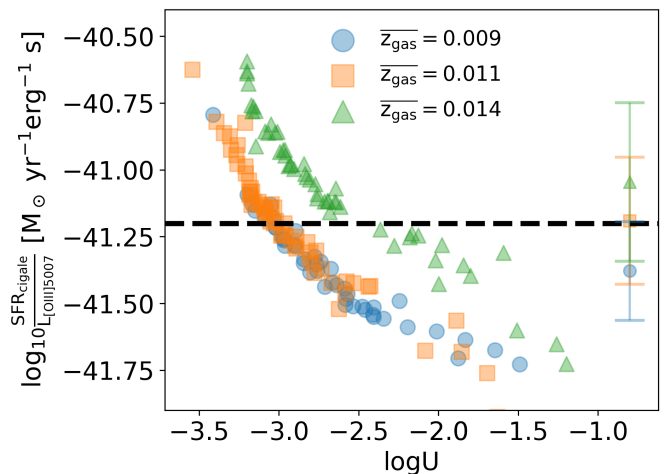


Fig. 19. SFR and $L_{[OIII]5007}$ ratio vs the ionization parameter. Each metallicity bin is presented as blue dots, orange squares, and green triangles. The ionization parameter is computed with CIGALE for each fixed metallicity case. The black dashed line corresponds to the $-41.20 [M_{\odot} \text{ yr}^{-1} \text{ erg}^{-1} \text{ s}]$ intercept found in Eq. 6. The symbols with errors represent the median values of the $SFR/L_{[OIII]5007}$ ratio for each metallicity. The ionization parameter has a larger impact on the dispersion than the gas-phase metallicity.

7. Summary and Conclusions

In this work, we perform SED fitting using CIGALE on an FMOS-COSMOS spectro-photometric sample covering UV-to-FIR continuum emission with 21 broad-band fluxes and emission lines at $z \sim 1.6$. A sample of 183 objects was selected to have flux measurements of both $H\alpha$ and [OIII] λ 5007 at $S/N > 3$ in the FMOS survey. From SED fitting of both photometric and $H\alpha$ fluxes, we estimate SFR and stellar mass, and constrain dust attenuation affecting the $H\alpha$ and [OIII] λ 5007 emission lines. We measure median values of the emission line attenuation of

Table 5. SFR- $L_{[\text{OIII}]\lambda 5007}$ ratio mean values in 0.5 dex log U bins for the three different metallicities.

Z_{gas}	0.009	0.011	0.014
	$\log_{10} \left(\frac{\text{SFR}_{\text{cigale}}}{L_{[\text{OIII}]\lambda 5007}} \right)$		
	$[\text{M}_{\odot} \text{ yr}^{-1} \text{ erg}^{-1} \text{ s}]$		
log U			
-2.0 -2.5	-41.54	-41.44	-41.25
-2.5 -3.0	-41.35	-41.31	-41.04
-3.0 -3.5	-41.15	-41.10	-40.78

$A_{\text{H}\alpha} = 1.16 \pm 0.19$ mag and $A_{[\text{OIII}]} = 1.41 \pm 0.22$ mag, respectively. Both $A_{\text{H}\alpha}$ and $A_{[\text{OIII}]}$ increase with stellar mass with a larger attenuation correction for $[\text{OIII}]\lambda 5007$ emission line as compared to $\text{H}\alpha$. We find a flatter effective attenuation curve than the Milky Way or C00 curves. A relation to obtain the attenuation for the $[\text{OIII}]\lambda 5007$ line as a function of stellar mass is proposed in the same way as it exists for $\text{H}\alpha$. This relation could be useful for inferring average values of the SFR of a sample, but not for individual galaxies. The relative attenuation affecting different populations is characterized by the μ parameter in the attenuation law. We find a value of $\mu = 0.57 \pm 0.14$ consistent with different works in the literature and twice as large as compared to the original value proposed by Charlot & Fall (2000).

A SFR- $L_{[\text{OIII}]\lambda 5007}$ dust-corrected relation is derived. We measure a slope consistent with unity within the 2σ dispersion of the relation. We estimate a $[\text{OIII}]\lambda 5007/[\text{OIII}] 88 \mu\text{m}$ ratio of 1.90 for our sample of galaxies and deduce a SFR- $[\text{OIII}] 88 \mu\text{m}$ relation in agreement with previous relations that were found at both low and high redshifts, although $[\text{OIII}]\lambda 5007/[\text{OIII}] 88 \mu\text{m}$ is strongly dependent on electron density and gas-phase metallicity. The SED fitting, including photometry, $\text{H}\alpha$, $\text{H}\beta$, and $[\text{OIII}]\lambda 5007$ fluxes, is also performed with a refined grid of photoionization models and metallicities estimated from the mass-metallicity relation from Curti et al. (2020). The variations of gas-phase metallicity and ionization parameter induce a dispersion in the SFR- $L_{[\text{OIII}]\lambda 5007}$ relation of 0.24 dex and 1.1 dex, respectively. The lower impact of gas-phase metallicity is likely to be due the limited range of our sample ($0.006 < Z_{\text{gas}} < 0.016$) and our relation of SFR- $L_{[\text{OIII}]\lambda 5007}$ is expected to be only valid for galaxies of similar gas-phase metallicities as those studied in this work.

Acknowledgements. We are grateful to Daichi Kashino for sharing the FMOS private catalog, and William Bowman, Alessia Longobardi, Yannick Rhoelly, Katarzyna Małek, Miguel Figueira, and Akio Inoue for useful conversations and discussion. We thank the anonymous referee for their insightful comments to improve the quality of this work. The project has received funding from Excellence Initiative of Aix-Marseille University - AMIDEX, a French “Investissements d’Avenir” program. It was supported by the Programme National “Physique et Chimie du Milieu Interstellaire” (PCMI) of CNRS/INSU with INC/INP co-funded by CEA and CNES. MB acknowledges FONDECYT regular grants 1170618 and 1211000.

References

Allen, M. G., Groves, B. A., Dopita, M. A., Sutherland, R. S., & Kewley, L. J. 2008, *ApJS*, 178, 20
 Álvarez-Márquez, J., Colina, L., Marques-Chaves, R., et al. 2019, *A&A*, 629, A9
 Andrews, B. H. & Martini, P. 2013, *ApJ*, 765, 140
 Andrews, S. K., Driver, S. P., Davies, L. J. M., Lagos, C. d. P., & Robotham, A. S. G. 2018, *MNRAS*, 474, 898

Arata, S., Yajima, H., Nagamine, K., Abe, M., & Khochfar, S. 2020, *MNRAS*, 498, 5541
 Arnouts, S., Cristiani, S., Moscardini, L., et al. 1999, *MNRAS*, 310, 540
 Asplund, M., Grevesse, N., Sauval, A. J., & Scott, P. 2009, *ARA&A*, 47, 481
 Baldwin, J. A., Phillips, M. M., & Terlevich, R. 1981, *PASP*, 93, 5
 Battisti, A. J., Calzetti, D., & Chary, R. R. 2016, *ApJ*, 818, 13
 Battisti, A. J., da Cunha, E., Grasha, K., et al. 2019, *ApJ*, 882, 61
 Bian, F., Kewley, L. J., Groves, B., & Dopita, M. A. 2020, *MNRAS*, 493, 580
 Boquien, M., Burgarella, D., Roehly, Y., et al. 2019, *A&A*, 622, A103
 Bourne, N., Maddox, S. J., Dunne, L., et al. 2012, *MNRAS*, 421, 3027
 Bowman, W. P., Zeimann, G. R., Ciardullo, R., et al. 2019, *ApJ*, 875, 152
 Bowman, W. P., Zeimann, G. R., Nagaraj, G., et al. 2020, *ApJ*, 899, 7
 Brinchmann, J., Pettini, M., & Charlot, S. 2008, *MNRAS*, 385, 769
 Bruzual, G. & Charlot, S. 2003, *MNRAS*, 344, 1000
 Buat, V., Boquien, M., Małek, K., et al. 2018, *A&A*, 619, A135
 Buat, V., Ciesla, L., Boquien, M., Małek, K., & Burgarella, D. 2019, *A&A*, 632, A79
 Byler, N., Dalcanton, J. J., Conroy, C., & Johnson, B. D. 2017, *ApJ*, 840, 44
 Calzetti, D., Armus, L., Bohlin, R. C., et al. 2000, *ApJ*, 533, 682
 Capak, P., Aussel, H., Bundy, K., et al. 2012, SPLASH: Spitzer Large Area Survey with Hyper-Suprime-Cam, Spitzer Proposal
 Caplan, J. & Deharveng, L. 1986, *A&A*, 155, 297
 Cardelli, J. A., Clayton, G. C., & Mathis, J. S. 1989, *ApJ*, 345, 245
 Carnall, A. C., Leja, J., Johnson, B. D., et al. 2019, *ApJ*, 873, 44
 Carnall, A. C., McLure, R. J., Dunlop, J. S., & Davé, R. 2018, *MNRAS*, 480, 4379
 Casey, C. M. 2012, *MNRAS*, 425, 3094
 Chabrier, G. 2003, *PASP*, 115, 763
 Charlot, S. & Fall, S. M. 2000, *ApJ*, 539, 718
 Chevallard, J. & Charlot, S. 2016, *MNRAS*, 462, 1415
 Chevallard, J., Curtis-Lake, E., Charlot, S., et al. 2019, *MNRAS*, 483, 2621
 Ciesla, L., Elbaz, D., & Fensch, J. 2017, *A&A*, 608, A41
 Civano, F., Marchesi, S., Comastri, A., et al. 2016, *ApJ*, 819, 62
 Corre, D., Buat, V., Basa, S., et al. 2018, *A&A*, 617, A141
 Cortese, L., Ciesla, L., Boselli, A., et al. 2012, *A&A*, 540, A52
 Cowie, L. L., Barger, A. J., & Songaila, A. 2016, *ApJ*, 817, 57
 Curti, M., Mannucci, F., Cresci, G., & Maiolino, R. 2020, *MNRAS*, 491, 944
 da Cunha, E., Charlot, S., & Elbaz, D. 2008, *MNRAS*, 388, 1595
 Dale, D. A., Helou, G., Magdis, G. E., et al. 2014, *ApJ*, 784, 83
 De Looze, J. L., Cormier, D., Lebouteiller, V., et al. 2014, *A&A*, 568, A62
 Dinerstein, H. L. 1983, in *Planetary Nebulae*, ed. L. H. Aller, Vol. 103, 79–88
 Dobbels, W., Baes, M., Viaene, S., et al. 2020, *A&A*, 634, A57
 Donley, J. L., Koekemoer, A. M., Brusa, M., et al. 2012, *ApJ*, 748, 142
 Dopita, M. A., Kewley, L. J., Sutherland, R. S., & Nicholls, D. C. 2016, *Ap&SS*, 361, 61
 Dopita, M. A., Sutherland, R. S., Nicholls, D. C., Kewley, L. J., & Vogt, F. P. A. 2013, *ApJS*, 208, 10
 Draine, B. T., Aniano, G., Krause, O., et al. 2014, *ApJ*, 780, 172
 Draine, B. T. & Li, A. 2007, *ApJ*, 657, 810
 Ellis, R. S., Bland-Hawthorn, J., Bremer, M., et al. 2017, arXiv e-prints, arXiv:1701.01976
 Elvis, M., Civano, F., Vignali, C., et al. 2009, *ApJS*, 184, 158
 Ferkinhoff, C., Hailey-Dunsheath, S., Nikola, T., et al. 2010, *ApJ*, 714, L147
 Ferland, G. J., Chatzikos, M., Guzmán, F., et al. 2017, *Rev. Mexicana Astron. Astrofis.*, 53, 385
 Fossati, M., Mendel, J. T., Boselli, A., et al. 2018, *A&A*, 614, A57
 Fritz, J., Franceschini, A., & Hatziminaoglou, E. 2006, *MNRAS*, 366, 767
 Garn, T. & Best, P. N. 2010a, *MNRAS*, 409, 421
 Garn, T. & Best, P. N. 2010b, *MNRAS*, 409, 421
 Grevesse, N., Asplund, M., Sauval, A. J., & Scott, P. 2010, *Ap&SS*, 328, 179
 Gutkin, J., Charlot, S., & Bruzual, G. 2016, *MNRAS*, 462, 1757
 Harikane, Y., Ouchi, M., Inoue, A. K., et al. 2020, *ApJ*, 896, 93
 Hippelein, H., Maier, C., Meisenheimer, K., et al. 2003, *A&A*, 402, 65
 Hurlley, P. D., Oliver, S., Betancourt, M., et al. 2017, *MNRAS*, 464, 885
 Ibar, E., Sobral, D., Best, P. N., et al. 2013, *MNRAS*, 434, 3218
 Ilbert, O., Arnouts, S., McCracken, H. J., et al. 2006, *A&A*, 457, 841
 Jin, S., Daddi, E., Liu, D., et al. 2018, *ApJ*, 864, 56
 Johnson, B. D., Leja, J., Conroy, C., & Speagle, J. S. 2021, *ApJS*, 254, 22
 Kaasinen, M., Kewley, L., Bian, F., et al. 2018, *MNRAS*, 477, 5568
 Karim, A., Schinnerer, E., Martínez-Sansigre, A., et al. 2011, *ApJ*, 730, 61
 Kashino, D., Silverman, J. D., Rodighiero, G., et al. 2013, *ApJ*, 777, L8
 Kashino, D., Silverman, J. D., Sanders, D., et al. 2019, *ApJS*, 241, 10
 Kashino, D., Silverman, J. D., Sanders, D., et al. 2017, *ApJ*, 835, 88
 Kauffmann, G., Heckman, T. M., Tremonti, C., et al. 2003, *MNRAS*, 346, 1055
 Kennicutt, Robert C., J. 1992, *ApJ*, 388, 310
 Kennicutt, Robert C., J. 1998, *ARA&A*, 36, 189
 Kennicutt, Robert C., J., Bresolin, F., French, H., & Martin, P. 2000, *ApJ*, 537, 589
 Kewley, L. J., Dopita, M. A., Leitherer, C., et al. 2013, *The Astrophysical Journal*, 774, 100

- Kewley, L. J., Dopita, M. A., Sutherland, R. S., Heisler, C. A., & Trevena, J. 2001, *ApJ*, 556, 121
- Kewley, L. J., Maier, C., Yabe, K., et al. 2013, *ApJ*, 774, L10
- Kojima, T., Ouchi, M., Nakajima, K., et al. 2017, *PASJ*, 69, 44
- Komatsu, E., Smith, K. M., Dunkley, J., et al. 2011, *ApJS*, 192, 18
- Koyama, Y., Shimakawa, R., Yamamura, I., Kodama, T., & Hayashi, M. 2019, *PASJ*, 71, 8
- Laigle, C., McCracken, H. J., Ilbert, O., et al. 2016, *ApJS*, 224, 24
- Le Floch, E., Aussel, H., Ilbert, O., et al. 2009, *ApJ*, 703, 222
- Leja, J., Carnall, A. C., Johnson, B. D., Conroy, C., & Speagle, J. S. 2019, *ApJ*, 876, 3
- Leja, J., Johnson, B. D., Conroy, C., van Dokkum, P. G., & Byler, N. 2017, *ApJ*, 837, 170
- Levesque, E. M., Kewley, L. J., & Larson, K. L. 2010, *AJ*, 139, 712
- Liu, G., Calzetti, D., Hong, S., et al. 2013, *ApJ*, 778, L41
- Lo Faro, B., Buat, V., Roehly, Y., et al. 2017, *MNRAS*, 472, 1372
- Lodders, K. 2010, *Astrophysics and Space Science Proceedings*, 16, 379
- Ly, C., Malkan, M. A., Kashikawa, N., et al. 2007, *ApJ*, 657, 738
- Małek, K., Buat, V., Roehly, Y., et al. 2018, *A&A*, 620, A50
- Mannucci, F., Cresci, G., Maiolino, R., Marconi, A., & Gnerucci, A. 2010, *MNRAS*, 408, 2115
- Maschietto, F., Hatch, N. A., Venemans, B. P., et al. 2008, *MNRAS*, 389, 1223
- Masters, D., Faisst, A., & Capak, P. 2016, *ApJ*, 828, 18
- Masters, D., McCarthy, P., Siana, B., et al. 2014, *ApJ*, 785, 153
- Moriwaki, K., Yoshida, N., Shimizu, I., et al. 2018, *MNRAS*, 481, L84
- Moustakas, J., Kennicutt, Robert C., J., & Tremonti, C. A. 2006, *ApJ*, 642, 775
- Nersesian, A., Xilouris, E. M., Bianchi, S., et al. 2019, *A&A*, 624, A80
- Nicholls, D. C., Sutherland, R. S., Dopita, M. A., Kewley, L. J., & Groves, B. A. 2017, *MNRAS*, 466, 4403
- Nieva, M. F. & Przybilla, N. 2012, *A&A*, 539, A143
- O'Donnell, J. E. 1994, *ApJ*, 422, 158
- Osterbrock, D. E. 1989, *Astrophysics of gaseous nebulae and active galactic nuclei* (University Science Books)
- Pannella, M., Elbaz, D., Daddi, E., et al. 2015, *ApJ*, 807, 141
- Pérez-Montero, E. 2014, *MNRAS*, 441, 2663
- Pettini, M. & Pagel, B. E. J. 2004, *MNRAS*, 348, L59
- Popescu, C. C., Misiriotis, A., Kylafis, N. D., Tuffs, R. J., & Fischera, J. 2000, *A&A*, 362, 138
- Puglisi, A., Rodighiero, G., Franceschini, A., et al. 2016, *A&A*, 586, A83
- Qin, J., Zheng, X. Z., Wuyts, S., Pan, Z., & Ren, J. 2019, *ApJ*, 886, 28
- Reddy, N. A., Kriek, M., Shapley, A. E., et al. 2015, *ApJ*, 806, 259
- Robotham, A. S. G., Bellstedt, S., Lagos, C. d. P., et al. 2020, *MNRAS*, 495, 905
- Rodighiero, G., Daddi, E., Baronchelli, I., et al. 2011, *ApJ*, 739, L40
- Sanders, R. L., Shapley, A. E., Jones, T., et al. 2021, *ApJ*, 914, 19
- Sanders, R. L., Shapley, A. E., Kriek, M., et al. 2016, *ApJ*, 816, 23
- Sanders, R. L., Shapley, A. E., Reddy, N. A., et al. 2020, *MNRAS*, 491, 1427
- Santini, P., Maiolino, R., Magnelli, B., et al. 2014, *A&A*, 562, A30
- Sargent, M. T., Béthermin, M., Daddi, E., & Elbaz, D. 2012, *ApJ*, 747, L31
- Schaerer, D. & de Barros, S. 2009, *A&A*, 502, 423
- Schaerer, D. & de Barros, S. 2010, *A&A*, 515, A73
- Schreiber, C., Pannella, M., Elbaz, D., et al. 2015, *A&A*, 575, A74
- Schwarz, G. 1978, *Annals of Statistics*, 6, 461
- Scoville, N., Aussel, H., Brusa, M., et al. 2007, *ApJS*, 172, 1
- Shapley, A. E., Reddy, N. A., Kriek, M., et al. 2015, *ApJ*, 801, 88
- Shimakawa, R., Kodama, T., Steidel, C. C., et al. 2015, *MNRAS*, 451, 1284
- Shivaei, I., Reddy, N., Rieke, G., et al. 2020, *ApJ*, 899, 117
- Silva, L., Granato, G. L., Bressan, A., & Danese, L. 1998, *ApJ*, 509, 103
- Silverman, J. D., Kashino, D., Sanders, D., et al. 2015, *ApJS*, 220, 12
- Smith, D. J. B., Dunne, L., da Cunha, E., et al. 2012, *MNRAS*, 427, 703
- Stacey, G. J., Hailey-Dunsheath, S., Ferkinhoff, C., et al. 2010, *ApJ*, 724, 957
- Stark, D. P., Schenker, M. A., Ellis, R., et al. 2013, *ApJ*, 763, 129
- Steidel, C. C., Rudie, G. C., Strom, A. L., et al. 2014, *ApJ*, 795, 165
- Steidel, C. C., Strom, A. L., Pettini, M., et al. 2016, *ApJ*, 826, 159
- Straughn, A. N., Pirzkal, N., Meurer, G. R., et al. 2009, *AJ*, 138, 1022
- Strom, A. L., Steidel, C. C., Rudie, G. C., et al. 2017, *ApJ*, 836, 164
- Tang, M., Stark, D. P., Chevallard, J., et al. 2021, *MNRAS*, 501, 3238
- Teplitz, H. I., Malkan, M. A., Steidel, C. C., et al. 2000, *ApJ*, 542, 18
- Theios, R. L., Steidel, C. C., Strom, A. L., et al. 2019, *ApJ*, 871, 128
- Thorne, J. E., Robotham, A. S. G., Davies, L. J. M., et al. 2021, *MNRAS*, 505, 540
- Topping, M. W., Shapley, A. E., Reddy, N. A., et al. 2020, *MNRAS*, 499, 1652
- Veilleux, S. & Osterbrock, D. E. 1987, *ApJS*, 63, 295
- Vila-Costas, M. B. & Edmunds, M. G. 1993, *MNRAS*, 265, 199
- Wells, M., Pel, J. W., Glasse, A., et al. 2015, *PASP*, 127, 646
- Wild, V., Kauffmann, G., Heckman, T., et al. 2007, *MNRAS*, 381, 543
- Wright, G. S., Wright, D., Goodson, G. B., et al. 2015, *PASP*, 127, 595
- Yabe, K., Ohta, K., Akiyama, M., et al. 2015, *PASJ*, 67, 102
- Yuan, F.-T., Burgarella, D., Corre, D., et al. 2019, *A&A*, 631, A123
- Zahid, H. J., Kudritzki, R.-P., Conroy, C., Andrews, B., & Ho, I. T. 2017, *ApJ*, 847, 18